

Self-regulated star formation in galaxies via momentum input from massive stars

Philip F. Hopkins,^{1★} Eliot Quataert¹ and Norman Murray^{2†}

¹*Department of Astronomy and Theoretical Astrophysics Center, University of California Berkeley, Berkeley, CA 94720, USA*

²*Canadian Institute for Theoretical Astrophysics, 60 St. George Street, University of Toronto, ON M5S 3H8, Canada*

Accepted 2011 June 21. Received 2011 June 21; in original form 2011 January 24

ABSTRACT

Feedback from massive stars is believed to play a critical role in shaping the galaxy mass function, the structure of the interstellar medium (ISM) and the low efficiency of star formation, but the exact form of the feedback is uncertain. In this paper, the first in a series, we present and test a novel numerical implementation of stellar feedback resulting from momentum imparted to the ISM by radiation, supernovae and stellar winds. We employ a realistic cooling function, and find that a large fraction of the gas cools to $\lesssim 100$ K, so that the ISM becomes highly inhomogeneous. Despite this, our simulated galaxies reach an approximate steady state, in which gas gravitationally collapses to form giant ‘molecular’ clouds (GMCs), dense clumps and stars; subsequently, stellar feedback disperses the GMCs, repopulating the diffuse ISM. This collapse and dispersal cycle is seen in models of Small Magellanic Cloud (SMC)-like dwarfs, the Milky Way and $z \sim 2$ clumpy disc analogues. The simulated global star formation efficiencies are consistent with the observed Kennicutt–Schmidt relation. Moreover, the star formation rates are nearly independent of the numerically imposed high-density star formation efficiency, density threshold and density scaling. This is a consequence of the fact that, in our simulations, star formation is regulated by stellar feedback limiting the amount of very dense gas available for forming stars. In contrast, in simulations without stellar feedback, i.e. under the action of only gravity and gravitationally induced turbulence, the ISM experiences runaway collapse to very high densities. In these simulations without feedback, the global star formation rates exceed observed galactic star formation rates by 1–2 orders of magnitude, demonstrating that stellar feedback is crucial to the regulation of star formation in galaxies.

Key words: galaxies: evolution – galaxies: formation – cosmology: theory.

1 INTRODUCTION

Feedback from massive stars plays a critical role in the evolution of galaxies. Cosmological models of galaxy evolution generically find that, without strong stellar feedback, the net stellar mass formed from cooled baryons exceeds that observed by an order of magnitude or more, particularly in lower mass haloes (e.g. Katz, Weinberg & Hernquist 1996; Somerville & Primack 1999; Cole et al. 2000; Springel & Hernquist 2003b; Kereš et al. 2009, and references therein). Related problems exist on smaller scales within galaxies. The observed relationship between star formation rate (SFR) density and gas surface density – the Kennicutt–Schmidt (KS) law – implies

that star formation is slow averaged over galaxies as a whole: the gas consumption time-scale is ~ 50 dynamical times (Kennicutt 1998), much longer than the naive estimate of \sim a few dynamical times one might expect in self-gravitating gas. Similar gas consumption times are found even in dense regions in galaxies (e.g. Krumholz & Tan 2007; but see also Schrubba et al. 2010; Feldmann & Gnedin 2011; Murray 2011). Moreover, observations in the Milky Way (MW) and nearby galaxies show that individual giant molecular clouds (GMCs) – the sites of star formation – convert only a few per cent of their mass into stars during their lifetimes (Zuckerman & Evans 1974; Williams & McKee 1997; Evans 1999; Evans et al. 2009). One of the leading explanations for this low star formation efficiency is that stellar feedback disrupts GMCs once enough stars have formed.

Numerical simulations of isolated galaxies and galaxy mergers, as well as cosmological ‘zoom-in’ simulations of individual haloes,

★E-mail: phopkins@astro.berkeley.edu

†Canada Research Chair in Astrophysics.

can now reach the resolution required to resolve the formation of GMCs, $\sim 1\text{--}100\text{ pc}$ (see e.g. Saitoh et al. 2008; Tasker & Tan 2009; Bournaud et al. 2010; Dobbs, Burkert & Pringle 2011) (note that GMCs in massive gas-rich galaxies are $\sim \text{kpc}$ in size, significantly larger than in the MW). If simulations do not, however, include physics that disrupts GMCs, they do not have a physically self-consistent model of the interstellar medium (ISM) on such scales. All of the gas will be unrealistically locked up in dense gaseous/stellar clusters, instead of being recycled back into the more diffuse ISM. Given resolution limitations, most recipes in galaxy and cosmological-scale simulations have been developed to treat star formation and feedback in a restricted ‘sub-grid’ manner. However, without more detailed models of this physics, it is difficult to assess how appropriate the sub-grid prescriptions are for different galaxy types. Moreover, the assumptions of such models break down and are no longer meaningful at the spatial ($\lesssim \text{pc}$) or time evolution ($\lesssim \text{Myr}$) scales of individual GMCs and ISM sub-structure. In particular, whenever a numerical simulation has the resolution to resolve the *formation* of bound gaseous structures like GMCs, we believe that it is equally critical to include physics that can potentially *disrupt* such GMCs.

Protostellar jets, H II regions, stellar winds, radiation pressure from young stars and supernovae (SNe) all appear to be important sources of feedback and turbulence in the ISM of galaxies. In regions of low-mass star formation it is likely that protostellar jets dominate, but for the ISM as a whole massive stars are the most important sources of feedback. In relatively low density gas, heating by photoionization, stellar winds and SNe is critical (McKee & Ostriker 1977; Matzner 2002). For denser gas, however, which often corresponds to most of the mass in a galaxy, energy deposition is ineffective; the cooling time [$\tau_{\text{cool}} = kT/\Lambda n \approx 3000(T/10^4 \text{ K})(1 \text{ cm}^{-3}/n) \text{ yr}$, where $\Lambda \approx 10^{-23} \text{ erg cm}^3 \text{ s}^{-1}$ is the cooling function] is short compared to the dynamical time for all but the lowest density gas, so the energy deposited into the gas by stellar feedback is rapidly radiated away. Even in the MW, the hot ISM contributes only ~ 10 per cent to the total ISM pressure (Boulares & Cox 1990). In contrast, the momentum supplied by stellar luminosity, winds and SNe cannot be radiated away, and is the most important source of feedback for dense gas in galaxies (e.g. Murray, Quataert & Thompson 2010).

Although it is widely believed that stellar feedback is critical for understanding the self-regulation of star formation within galaxies, and for the cosmological evolution of galaxies themselves, it is quite challenging to treat this in galaxy-scale simulations, especially with the computational limitations faced by previous generations of simulations. As a result, many simulations have made the problem tractable by adopting effective equation of state models in which feedback processes are treated implicitly (e.g. Springel & Hernquist 2003a; Teyssier, Chapon & Bournaud 2010), accounting for the (un-resolved) multi-phase turbulent structure of the ISM with an ‘effective’ high sound speed. Unfortunately, in this case many of the net effects of stellar feedback are then put in by hand – one cannot predict, e.g. either how efficient feedback is in different systems or whether stellar feedback drives galactic winds. More broadly, without simulations that explicitly model feedback, it is difficult to evaluate the accuracy of the various sub-grid treatments in the literature.

Galactic-scale simulations that do include stellar feedback explicitly have often been forced to alter the physics in significant ways in order to obtain a desired result. The most common treatment is to only include thermal gas heating from SNe. However, thermal feedback is very inefficient in the dense regions where star

formation occurs, and in the ISM more broadly in starbursts and gas-rich high-redshift galaxies. These problems are compounded when simulations cannot resolve the ISM phase structure, and smooth together dense GMCs and diffuse gas into a single average density (greatly increasing/decreasing the cooling time in dense/diffuse gas, respectively). For this reason, in order to make SN feedback have any significant effect (even in MW-like galaxies), simulators often ‘turn-off’ cooling (often along with star formation and/or other hydrodynamic processes) for an extended period of time, much longer than τ_{cool} (cooling is typically suppressed for $\sim 10^7\text{--}10^8 \text{ yr}$, i.e. for a time comparable to a galaxy dynamical time and $\sim 10^4$ times longer than the actual cooling time at the same density; see e.g. Thacker & Couchman 2000; Governato et al. 2007; Brook et al. 2011). Other models explicitly disable certain interactions between gas flagged as ‘cold’ and ‘hot’ or deposit feedback energy in a non-cooling reservoir that serves to move gas from cold to hot phases (Scannapieco et al. 2008). Even with these adjustments, many such models have found it difficult to drive winds and suppress star formation at the level needed to explain the galaxy mass function (especially at low masses) and observed star formation efficiencies (see e.g. Guo et al. 2010; Powell, Slyz & Devriendt 2011; Brook et al. 2011; Nagamine 2011, and references therein).

Simulations with SN feedback that do not ‘turn-off’ cooling have found that galactic outflows can only be driven if additional physics is included. For example, Ceverino & Klypin (2009) were able to drive galactic winds by requiring that SNe explode well outside of the GMCs in which they formed. However (as they acknowledge), although this may well be important for galactic winds, it leaves the problem of locally preventing runaway collapse of dense star-forming regions.

The inefficiency of SN heating in dense gas is physically correct.¹ It is thus by no means clear that turning off cooling is an appropriate resolution of the ‘problem’ that SN remnants cool! Instead, we believe that this points to the importance of including the momentum supplied by stellar feedback processes. This momentum input into the ISM can drive strong turbulence and can itself contribute to unbinding gas from galaxies, even in the limit of very rapid cooling (Murray, Quataert & Thompson 2005). To date, however, this has only been treated in a phenomenological way, given the limited resolution of previous simulations. In particular, in a widely used implementation in the GADGET smoothed particle hydrodynamics (SPH) code, gas particles are ‘kicked’ into a ‘wind’ at a rate proportional to either the SFR or young stellar mass, with the wind velocity set by hand as a constant or a multiple of the galaxy escape velocity (Springel & Hernquist 2003a; Dalla Vecchia & Schaye 2008; Oppenheimer & Davé 2008; Sales et al. 2010; Genel et al. 2010). All hydrodynamic interactions (e.g. shocks and pressure forces) for the ‘wind particles’ are turned off until they escape the galaxy (and when this is not done, the effects of winds are substantially suppressed; Sales et al. 2010). This model is useful for studying the impact of galactic outflows on the intergalactic medium and the galaxy mass function but it is clearly limited (especially within galaxies) and cannot predict the nature and origin of these winds.

Motivated by these considerations, this is the first in a series of papers studying stellar feedback in numerical models of galaxies and the resulting implications for problems such as the origin of

¹ It is, of course, true that simulations do not resolve the full multi-phase ISM into which SNe propagate and that this can enable SN energy to propagate to larger distances.

Table 1. Galaxy models.

Model	ϵ_g (pc)	m_i (M_\odot)	M_{halo} (M_\odot)	c	V_{max} (km s^{-1})	M_{bary} (M_\odot)	M_b (M_\odot)	a (kpc)	M_d (M_\odot)	r_d (kpc)	h (pc)	M_g (M_\odot)	r_g (kpc)	f_{gas}	t_{dyn} (Myr)
Sbc	2.5	130	1.5e11	11	86	1.05e10	1e9	0.35	4e9	1.3	320	5.5e9	2.6	0.36	22
HiZ	3.5	1700	1.4e12	3.5	230	1.7e11	7e10	1.2	3e10	1.6	130	7e10	3.2	0.49	12
MW	2.5	220	1.6e12	12	190	7.13e10	1.5e10	1.0	4.73e10	3.0	300	0.9e10	6.0	0.09	31
SMC	0.7	25	2.0e10	15	46	8.9e8	1e7	0.25	1.3e8	0.7	140	7.5e8	2.1	0.56	45

Parameters describing our galaxy models, used as the initial conditions for all of the simulations:

(1) model name: shorthand for models of a high-redshift massive starburst (HiZ), local gas-rich galaxy (Sbc), MW-analogue (MW) and isolated SMC-mass dwarf (SMC). (2) ϵ_g : gravitational force softening in our highest-resolution simulations (ultra-high-resolution). ‘High-resolution’ simulations use twice this value. ‘Intermediate-resolution’ four times this value. (3) m_i : gas particle mass in our highest-resolution simulations (ultra-high-resolution). ‘High-resolution’ simulations use eight times this value. ‘Intermediate-resolution’ 50 times this value. New star particles formed have mass $=0.5 m_i$, disc/bulge particles $\approx m_i$ and dark-matter halo particles $\approx 5 m_i$. (4) M_{halo} : halo mass. (5) c : halo concentration. Values lie on the halo mass–concentration relation at each redshift ($z = 0$ for SMC, Sbc and MW; $z = 2$ for HiZ). (6) V_{max} : halo maximum circular velocity. (7) M_{bary} : total baryonic mass. (8) M_b : bulge mass. (9) a : Hernquist (1990) profile scalelength for bulge. (10) M_d : stellar disc mass. (11) r_d : stellar disc scalelength. (12) h : stellar disc scaleheight. (13) M_g : gas disc mass. (14) r_g : gas disc scalelength (gas scaleheight determined so that $Q = 1$). (15) f_{gas} : average gas fraction of the disc inside of the stellar R_e ($M_g[<R_e]/(M_g[<R_e] + M_d[<R_e])$). The total gas fraction, including the extended disc, is ~ 50 per cent larger. (16) t_{dyn} : gas disc dynamical time at the half-gas mass radius.

galactic winds, the physics of gas inflow in galaxy mergers and the properties of the ISM in high-redshift galaxies.² Ultimately, we will present results that include simple models of SN heating, H II regions and radiation pressure from massive stars (produced by the absorption and scattering of UV and IR radiation on dust). Feedback from a central active galactic nucleus may also be important for understanding some aspects of star formation in galaxies – particularly the cessation of star formation in massive galaxies – but this is a separate problem that we do not consider in this paper.

It is still not currently computationally feasible to include all of the physics of stellar feedback in simulations that focus on galactic scales. The methods we develop therefore still rely on sub-grid models, but at the sub-cluster or sub-GMC scale, as opposed to the galaxy scale. The fact that different feedback processes dominate under different physical conditions (e.g. density) highlights the importance of including a range of physical processes when studying the effects of stellar feedback on galaxies and galaxy formation. None the less, in this paper, we focus on isolated (non-cosmological) galaxies and only include feedback by momentum deposition from massive stars. Our motivation for doing so is several-fold. First, our model for momentum deposition is sufficiently different from existing treatments of stellar feedback in the literature that it requires a detailed explanation. More importantly, however, we show that this simple model is, by itself, able to explain the KS relation and the low star formation efficiency in galaxies. Moreover, the SFRs in our model galaxies typically change by less than a factor of ~ 2 when we include additional feedback processes (though other properties of the galaxies can change substantially, such as the morphology and phase structure of the ISM – this is particularly true for low-mass galaxy models).

The remainder of this paper is organized as follows. In Section 2 we describe our method of implementing feedback due to the injection of momentum by young, massive stars. The Appendix contains tests varying some of the parameters of our numerical method. The galaxy models we study are described in Table 1 and Section 2.3. We then summarize our key results on the star formation histories and structural properties of our model galaxies (Section 3). In Section 4 we show that these results do not depend strongly on the physics of star formation at high densities, the uncertain feedback

parameters and numerical resolution. We then show that our model galaxies are consistent with the observed KS relation (Section 5). Finally, in Section 6 we summarize our results and discuss their implications.

2 METHODOLOGY

The methods we present are general and can be implemented in both Eulerian and Lagrangian simulations. The specific simulations we carried out were performed with the parallel TREE-SPH code GADGET-3 (Springel 2005), based on a conservative formulation of SPH, which conserves energy and entropy simultaneously even when smoothing lengths evolve adaptively (see e.g. Hernquist 1993; Springel & Hernquist 2002; O’Shea et al. 2005). The detailed numerical methodology is described in Springel (2005), Springel & Hernquist (2003a) and Springel, Di Matteo & Hernquist (2005). Our simulations include stars, dark matter and gas, with new implementations of stellar feedback; we describe the salient features of this additional physics below. These calculations do not include models of black hole growth and feedback.

2.1 Cooling and star formation

In order to resolve the formation of very dense clumps, we extend the standard atomic+metal line cooling curves in GADGET (which cut off when the gas becomes neutral at $< 10^4$ K) to allow cooling by fine structure lines. Specifically, we tabulate the cooling function $\Lambda(T)$ from 1 to 10^4 K with CLOUDY, for a medium with density $n = 1 \text{ cm}^{-3}$, solar abundances and with an ionizing background matching that at $z = 0$.³ This is similar to the approach in a number of other simulations (see e.g. Robertson & Kravtsov 2008; Wise & Abel 2008; Ceverino & Klypin 2009) and gives identical results to the tabulated $\Lambda(T)$ presented in Sánchez-Salcedo, Vázquez-Semadeni & Gazol (2002). We are not attempting to follow the ISM chemistry and thus ignore the dependence of the cooling on abundance and radiation field. For our problems of interest, the cooling rates even at these

² Movies of these simulations are available at <https://www.cfa.harvard.edu/~phopkins/Site/Research.html>

³ Recalibrating our ‘baseline’ $\Lambda(T)$ at $n = 100 \text{ cm}^{-3}$ gives indistinguishable results. The difference (modulo the standard n^2 dependence) is much smaller than more dramatic cooling curve variations we consider among other numerical tests in Appendix A, which all produce nearly identical results because, in all cases, the cooling time is much less than the dynamical time.

low temperatures are uniformly much shorter than the dynamical times in all the systems we model; therefore, even large (factor ~ 5) changes in the cooling curve make no significant difference to our conclusions (we have checked this explicitly).

Because we allow cooling to very low temperatures, we also must account for finite simulation resolution by including a pressure floor to prevent artificial numerical fragmentation when the Jeans mass is not resolved (Truelove et al. 1997). We adopt the prescription in Robertson & Kravtsov (2008), which ensures that the Jeans length is always resolved with N_{Jeans} smoothing lengths. This density-dependent pressure floor is

$$P_{\text{Jeans}} \approx 1.2 N_{\text{Jeans}}^{2/3} \gamma^{-1} G h_{\text{sml}}^2 \rho^2, \quad (1)$$

where $\gamma = 5/3$, ρ is the local density and h_{sml} the smoothing length. We typically adopt $N_{\text{Jeans}} = 10$, but have experimented with $N_{\text{Jeans}} = 4$ –15 and find similar results [the morphologies, SFRs and Schmidt–Kennicutt relations are indistinguishable; see Appendix A]. We make one small modification to the prescription in Robertson & Kravtsov (2008), which is to track the numerical pressure floor separately so that it enters into the momentum equations, but does not explicitly change the gas temperature (relevant, e.g., for determining the cooling function). This is a standard approach in high-resolution simulations (see e.g. Teyssier et al. 2010). At the typical resolution we adopt, the pressure provided by equation (1) is much less than the turbulent pressure resulting from our feedback model (by a factor of $\sim 10^2$ – 10^4); only when we turn-off feedback entirely is the ISM pressure resolution-limited.

In our simulations, stars are assumed to form from dense gas with a constant efficiency ϵ per free-fall time $t_{\text{ff}} = \sqrt{3\pi/32} G \rho$, above some minimum threshold ρ_0 , i.e.

$$\dot{\rho}_* = \frac{\epsilon \rho}{t_{\text{ff}}} \propto \rho^{3/2} \text{ for } \rho > \rho_0. \quad (2)$$

This is numerically implemented by turning gas particles into stars stochastically following the calculated SFR [probability $p = 1 - \exp(-\dot{\rho}_* dt / \rho)$, where $dt \lesssim 100$ – 1000 yr is the simulation time-step and also represents how frequently these values are updated]. Because we wish to resolve the dense regions of star formation, we typically set $n_0 = 100 \text{ cm}^{-3}$, characteristic of large GMCs. The efficiency ϵ is empirically measured in dense star-forming regions to be ≈ 1 – 2 per cent, roughly constant over a wide range of densities ~ 10 – 10^6 cm^{-3} (Krumholz & Tan 2007); we adopt a canonical value of $\epsilon = 1.5$ per cent (see also Leroy et al. 2008). We discuss variations about these fiducial choices in Section 4.1.

2.2 Stellar feedback

For the reasons summarized in Section 1, we model stellar feedback by depositing momentum into the gas around young star clusters. This in turn drives strong turbulence in the ISM. For standard IMFs (e.g. Kroupa 2002), the momentum supplied to the ISM by stellar winds, SNe and the luminosity of young stars is all comparable (Leitherer et al. 1999; Murray et al. 2005). If SNe undergo a significant Sedov–Taylor phase, the Pressure–Volume (P–dV) work done can increase their momentum by a factor of ~ 10 (e.g. Thornton et al. 1998). Likewise, if the ISM is optically thick to the infrared radiation produced when dust reradiates stellar UV photons, the radiation energy density builds up, increasing the radiation pressure force by a factor of the infrared optical depth τ_{IR} . Modelling these processes in detail is a daunting task and one that is beyond the scope of this paper. Instead, we explore the general properties of models in which turbulence driven by momentum deposition is the dominant stellar feedback mechanism. This is a plausible approximation

even in the MW, since the hot ISM contributes only ~ 10 per cent to the ISM pressure (Boulares & Cox 1990). Moreover, in the well-studied star-forming region 30 Doradus in the Large Magellanic Cloud (LMC), observations directly implicate radiation pressure as the dominant mechanism of stellar feedback (Lopez et al. 2011). We stress, however, that this is not intended to represent a complete model of stellar feedback and the ISM; in future work, we will study how galaxy properties are further modified with the addition of other mechanisms such as SNe and stellar wind shock heating and mass loss, and photoionization heating.

In order to make our simplified feedback model as realistic as possible, we implement the feedback so that it is explicitly associated with young star clusters. We do so by identifying star-forming clumps and depositing momentum into the surrounding gas radially away from the star clusters. In the following sections we describe the key steps in this method.

2.2.1 Star-forming clumps: identification

The first step is to identify star-forming regions or nascent star clusters in the simulation. Starting from each gas particle, we identify the nearest dense gas ‘clump’ by iteratively performing a friends-of-friends search with an adaptive linking length. Specifically, we search over all gas particles within a radius $N_{\text{sml}} h_{\text{sml}}$ (with typical $N_{\text{sml}} = 3$) of the initial particle to find that particle with the highest local density, and iterate either until a higher-density neighbour is not found or until some maximum cut-off is reached. For the latter we adopt a maximum of 20 iterations or a distance > 20 times the initial particle h_{sml} (in practice, this limit is rarely reached, but is necessary to prevent cases where, e.g., the linking chain might traverse a large fraction of the length of a spiral arm). Some care is needed in choosing the appropriate value of N_{sml} , based on the physical scales that are or are not resolved in a given simulation – for our resolutions, $N_{\text{sml}} < 1$ will simply return the local gas particle, and $N_{\text{sml}} \gg 5$ tends to over-link clumps in dense regions such as spiral arms and galactic nuclei. Our experiments show that within the range $N_{\text{sml}} \sim 1.5$ – 4 the identification of the peak local density is converged for > 90 per cent of all ‘clumps’ (with the remainder making little difference in global quantities, as we show explicitly in the Appendix); the density peaks identified in this way also agree well with visual identification of overdensities. We thus adopt a canonical value of $N_{\text{sml}} = 3$.

This friends-of-friends search defines the star-forming clump of which the initial gas particle is a member.⁴ The distance between the original particle and the clump centre (the clump density peak) defines the ‘clump radius’ R_{clump} (if this distance is less than twice the initial smoothing length, we set it to this minimum value, since the ‘clump’ is effectively unresolved). The enclosed ‘clump mass’ in gas ($M_{\text{clump, gas}}$) or stars ($M_{\text{clump, *}}$) is defined as the mass of each component within a distance of R_{clump} of the clump centre.

⁴ We have also experimented with using the centre of stellar light or the stellar density peak as the location of the clump centre (see the Appendix for details). In the systems we model here, there is no detectable difference between these choices and our fiducial choice of centring the clump on the peak gas density. However, the distinction between peak gas and stellar quantities could be more important in systems where the main-sequence lifetime exceeds the dynamical time (e.g. galactic nuclei) and massive stars may wander away from their natal GMCs.

2.2.2 Momentum loading

In our model, stellar feedback is tied to the properties of the stars in the stellar cluster associated with a given gas particle. Moreover, we only apply the feedback to gas particles that are within $3 h_{\text{sml}}$ of a young star particle (typically $\lesssim 10$ pc). This helps ensure that the feedback is spatially correlated with young stars.⁵ We now motivate our implementation in terms of feedback by radiation pressure on dust grains.

At each time-step, we identify the stars (of those formed since the beginning of the simulation) within the previously identified clump, and sum their bolometric luminosity, which is a function of the star's (known) stellar age

$$L_{\text{tot}}(< R_{\text{clump}}) = \sum_i^{r < R_{\text{clump}}} \left[\frac{L}{M}(\text{age}_i) \right] \times M_{*,i}. \quad (3)$$

We tabulate L_*/M_* as a function of age using a STARBURST99 (Leitherer et al. 1999) single stellar population with a Kroupa (2002) IMF at solar metallicity (this time dependence can be important on GMC time-scales, in contrast to models where all energy is coupled instantaneously; see e.g. Slyz et al. 2005). Given the uncertainties in the mass-loading factors below, and the fact that our initial conditions are all relatively evolved systems, it makes little difference whether we explicitly allow for a metallicity dependence.⁶ Assuming that the stellar flux is equally distributed among all of the gas within R_{clump} , we obtain the luminosity L_j incident on the particle in question, which has a mass $M_{\text{gas},j}$:

$$L_j = L_{\text{tot}}(< R_{\text{clump}}) \frac{M_{\text{gas},j}}{M_{\text{tot,gas}}(< R_{\text{clump}})}. \quad (4)$$

Because the luminosity incident on a particle in this simple formulation depends on the light-to-mass ratio of the surrounding stars, we find that our results are relatively insensitive to whether we use the starlight within R_{clump} or some multiple of this radius.

Given the incident luminosity, we take the rate of momentum deposition in the gas to be

$$\dot{p}_j = (1 + \eta_p \tau_{\text{IR}}) \frac{L_j}{c}. \quad (5)$$

This is the core equation of our feedback model (with typical values of τ_{IR} in Fig. 5). This force is directed radially away from the clump centre (i.e. along the vector $\mathbf{R}_{\text{clump}}$). If the particle j itself is the clump centre, the direction of the force is randomly chosen isotropically.

The first factor of L_j/c in equation (5) represents the momentum imparted as the optical-UV photons emitted by massive stars are absorbed by dust, which re-radiates in the IR. The factor of $\tau_{\text{IR}} L_j/c$ accounts for the momentum imparted by the total number of IR photons absorbed/scattered within the gas parcel. Note that τ_{IR} is the optical depth through the clump, not the optical depth of the given gas particle. It is the former that sets the total momentum supplied to the gas. Finally, equation (5) includes a dimensionless factor $\eta_p \sim$

1 that accounts for other sources of momentum and uncertainties introduced by our simplified treatment. Note, e.g., that we do not explicitly include the momentum deposited by stellar winds and SNe separately from that due to the radiation of massive stars; $\eta_p \gtrsim 1$ crudely accounts for these additional contributions.⁷ On the other hand, $\eta_p \lesssim 1$ might be appropriate if photons efficiently leak out through holes in the gas distribution (see Appendix B).

Why do we associate the feedback with the clump and direct it from that centre of density, as opposed to simply identifying it with each star individually? Recall, we are modelling the effects of radiation pressure in the limit in which the gas is at least somewhat optically thick. If the UV/optical photons could free-stream, then the appropriate sources would indeed be each star particle. However, if a number of stars are embedded in a gas clump, then in the limit of large optical depth, all of the stellar luminosity is trapped and re-radiated, so that the momentum flux is everywhere the full $d\tau L/c$ directed radially from the clump centre of density and follows the scalings we adopt here. This is trivially true in spherical or cylindrical (filamentary) geometries, but is a good approximation even for complex density distributions if the optical depths are sufficiently large. This is an important distinction that makes radiation pressure a particularly efficient feedback mechanism in dense regions (relative to other sources of energy or momentum such as SNe or stellar winds). In Appendix B we discuss the more complicated case of an inhomogeneous density distribution. However, to the extent that it modifies our conclusions, it is usually equivalent to variations in the net efficiency (encapsulated in η_p), rather than the spatial distribution or direction of the flux. Of course, if desired, the momentum could be isolated to each star by simply taking the limit $N_{\text{sml}} \rightarrow 0$.⁸

Given that the local density structure of the gas is at least partially resolved, we use this information to estimate the IR optical depth $\tau_{\text{IR}} = \Sigma_{\text{eff}} \kappa_{\text{IR}}$ where $\Sigma_{\text{eff}} \simeq M_{\text{clump}}/\pi R_{\text{clump}}^2$ is the gas surface density of the clump of interest.⁹ The opacity at IR wavelengths is approximately constant for dust temperatures ~ 100 – 1000 K, so we adopt $\kappa_{\text{IR}} \approx 5 \text{ cm}^2 \text{ g}^{-1}$ (this is convenient given that we are not performing radiative transfer and thus do not have information about the true dust temperature). Note that both the weighting of L_j and this calculation of τ_{IR} implicitly scale so that gas near the density centre where the flux and optical depth are largest will be more strongly accelerated than gas in the outskirts of the system.

We can apply the force associated with \dot{p}_j from equation (5) in two ways, either stochastically or as a continuous acceleration (the latter is the simplest to implement in grid-based calculations). In the stochastic model, we model the momentum deposition by randomly ‘kicking’ particles, with an average mass flux set by

$$\dot{M}_w v_w = \dot{p}_j, \quad (6)$$

⁷ We have considered experiments where we include a separate, explicit \dot{p}_j term for the direct momentum flux from stellar winds and SNe ejecta, with both tabulated in STARBURST99 as a function of stellar age. The absolute magnitude of these is, for a constant SFR, $\sim L/c$. We find this makes no difference compared to equivalent variation in η_p .

⁸ In Appendix A we show that directing the momentum from the cloud density peak, centre of gas mass or centre of stellar mass or luminosity makes no difference to our conclusions. Likewise allowing for more complex geometries by directing momentum along the local density gradients gives nearly identical results.

⁹ For an LN density distribution within a given clump, the effective optical depth of the inhomogeneous clump is typically within 30 per cent of the mean optical depth (Murray et al. 2010). Thus, using the latter to determine \dot{p}_j is sufficiently accurate for our purposes (see also Section 3.3).

⁵ Because the momentum deposition falls off for gas further from the stars, formally extending this to all of the gas makes no difference to our results.

⁶ We neglect for now the fact that at extremely high resolution, a $< 100 M_\odot$ ‘star particle’ may not completely sample the stellar IMF, and simply take the average L_*/M_* for the particle age. Since we focus on galaxy-average quantities, this is probably not a large uncertainty. But in low-mass clusters and GMCs, a more accurate model – for example one which the stellar mass range of each particle is sampled stochastically from the IMF, as discussed in Mashchenko, Wadsley & Couchman (2008) – could give interesting differences.

where \dot{M}_w is the mass loading and v_w is the initial velocity. What is the appropriate ‘initial’ velocity v_w ? Models of momentum-driven outflows argue that gas should be accelerated to the *local* escape velocity from the star clusters and/or clouds from which they are launched (Murray et al. 2010). We therefore take

$$v_w \approx v_{\text{esc}} \approx \eta_v v_{\text{dim}}(M_{\text{clump}}, \rho, \dots), \quad (7)$$

where v_{dim} is an estimate of the escape velocity as a function of the simulation parameters and η_v is a normalization parameter that accounts for details such as the exact mass profile shape, micro-physical acceleration as a function of position, etc. In practice, we have experimented with a variety of choices for the velocity and will show that it makes relatively little difference. This is because the key parameter that determines the effect of the feedback is the total momentum/force (equation 5).

The escape velocity from the clump as resolved by our simulations is $v_{\text{dim}} \approx \sqrt{2GM_{\text{clump}}/R_{\text{clump}}}$. However, some fraction of the clump will turn into stars in a dense stellar cluster, the internal dynamics and peak density of which are unresolved. The true relevant escape velocity from the location where the outflows are driven is probably the escape velocity from that cluster. We therefore take the mass in young stars in the clump to be the ‘star cluster’ mass and use the empirical size–mass relation of clusters (e.g. Murray 2009) to determine the cluster escape velocity:

$$v_{\text{dim}} = \left(\frac{2GM_{*,\text{cl}}}{R_{\text{cl}}} \right)^{1/2} \approx 66 \left(\frac{M_{*,\text{cl}}}{10^6 M_{\odot}} \right)^{1/4} \text{ km s}^{-1} \quad (8)$$

for $M_{*,\text{cl}} \sim 10^5$ – $10^9 M_{\odot}$. In our models, we take v_{dim} to be the maximum of either the resolved clump escape velocity or the inferred star cluster escape velocity; the latter is almost always larger. In a time-step Δt , the probability that the particle of mass $M_{\text{gas},j}$ is ‘kicked’ is then given by

$$P_w = 1 - \exp\{-\langle \dot{M}_w \Delta t \rangle / M_{\text{gas},j}\}. \quad (9)$$

The particle then has a momentum $\Delta p_j = M_{\text{gas},j} v_w$ added to its initial momentum, directed radially away from the clump centre.

In addition to the stochastic acceleration of particles described above, we can alternatively accelerate the particles continuously rather than with individual ‘kicks’; in this case the particle is simply given a $\Delta v_j = \dot{p}_j \Delta t / M_{\text{gas},j}$ every time-step. Which prescription is more physically appropriate depends on whether the outflows generated by stellar feedback are being accelerated at reasonably large radii (e.g. at the outskirts of clouds), or whether they are launched in the dense central regions near the star cluster. We show below that the two methods yield similar results.

Many implementations of stellar feedback in the literature turn-off the hydrodynamics, pressure forces, cooling and/or star formation for some period of time, often chosen such that a wind escapes the galaxy entirely (or until the wind reaches some distance from its launching point; see Springel & Hernquist 2003a; Oppenheimer & Davé 2008; Sales et al. 2010). In our models, by contrast, there is no such modification of the underlying equations. We are able to directly model the feedback and the resulting dissolution of star clusters for three reasons: first, our high resolution allows us to resolve a multi-phase ISM structure into which outflows can propagate; secondly, we identify massive star-forming regions and drive outflows coherently from them, rather than randomly within those regions; and thirdly, because the feedback is momentum-driven, it drives strong turbulence even in dense, highly radiative environments. In situations where a lower resolution is inevitable (e.g. cosmological simulations), it may be necessary for numerical reasons to modify the methods proposed here in order to maintain an

efficient source of stellar feedback. This will be studied in future work.

The feedback model used in this paper is ultimately defined by the two key parameters η_p and η_v (equations 5 and 7). We will discuss the consequences of different choices for these parameters below; we take $\eta_p \sim 1$ and $\eta_v \sim 1$ as our physically motivated default values.

2.3 Galaxy models

Our goal in this paper is to study the effects of stellar feedback on the ISM structure and star formation in galaxies. We do so using idealized models of disc galaxies with initial conditions motivated by galaxies in both the local and high-redshift Universe. We do not attempt to model the cosmological evolution of these discs, and so do not include extended gaseous haloes or cold flows from which they would accrete. Rather, our goal is to study how a given feedback mechanism will change behaviour given a specific set of (observed) disc properties. The methodology for building the initial galaxies follows that described in detail in a series of papers (see e.g. Di Matteo, Springel & Hernquist 2005; Springel et al. 2005; Cox et al. 2006; Robertson et al. 2006; Younger et al. 2008). The discs each include an extended dark-matter halo with an NFW profile (Navarro, Frenk & White 1996), a stellar bulge (typically with a Hernquist 1990 profile), and exponential stellar and gaseous discs. In all of the models, the initial vertical pressure support for the gas disc is provided by thermal pressure. As we describe in Sections 3 and 4, however, this thermal energy is quickly radiated away and the system approaches a new statistical equilibrium with star formation and stellar feedback determining many of the properties of the gas disc.

The simulations are carried out at several different resolutions: the ‘standard’ resolution has a total of $\approx 3 \times 10^6$ particles, with $\approx 10^6$ particles in the gas+stellar disc (the initial bulges are small and so have fewer particles – thus most of the remaining particles are in the dark-matter halo). Our ‘high’ resolution simulations use 10 times as many particles, reaching $\approx 10^7$ particles in the disc. We also have at least one ‘ultra-high’ resolution simulation per galaxy model with $> 10^8$ particles in the disc (to our knowledge, these are the highest-resolution galaxy-scale SPH simulations that have been performed to date). The models are generally all run for ≈ 20 dynamical times at R_e (≈ 3 orbital times), but they typically converge to quasi-steady-state behaviour after just ≈ 4 – $5 t_{\text{dyn}}$. After this the evolution is essentially just slow, steady-state gradual gas exhaustion; we have confirmed this in at least one run of each galaxy model run for five times longer than the ‘standard’ runs. As described below, the spatial and mass resolutions in each of the simulations depend on the galaxy model.

We consider four galaxy models, motivated by $z \sim 2$ high SFR galaxies (non-major mergers), local low-luminosity Luminous Infrared Galaxies (LIRGs), MW-like spirals and Small Magellanic Cloud (SMC)-like dwarf galaxies. The basic properties of these models are summarized in Table 1.

Sbc. This simulation is designed to model an intermediate-mass, relatively gas-rich star-forming disc in the local universe (e.g. a low-luminosity LIRG with $L_{\text{bol}} \sim 10^{10-11} L_{\odot}$ and $\dot{M} \sim 1$ – $10 M_{\odot} \text{ yr}^{-1}$). The galaxy has a total baryonic mass $1.05 \times 10^{10} M_{\odot}$, with a bulge having a mass $M_b = 10^9 M_{\odot}$ and a Hernquist (1990) scalelength $a = 350$ pc; a stellar disc with a mass $M_d = 4 \times 10^9 M_{\odot}$ and an exponential scalelength of $r_d = 1.3$ kpc; and an extended gaseous disc with $M_g = 5.5 \times 10^9 M_{\odot}$ and an exponential scalelength of $r_g = 2.6$ kpc. The stellar disc has a sech^2 vertical

profile with a scaleheight of 130 pc; it is initialized with a radial dispersion profile so that the local Toomre $Q = 1$ at all positions. The gas disc is similarly initialized in vertical hydrostatic equilibrium with $Q = 1$. The initial vertical support of the gas disc is via thermal pressure. The dark-matter halo has a virial mass $M_{\text{halo}} = 1.5 \times 10^{11} M_{\odot}$, concentration $c = 11$ and a spin parameter $\lambda = 0.033$, chosen to match the typical concentrations and spins seen in cosmological simulations (Bullock et al. 2001; Vitvitska et al. 2002); this gives a total stellar-to-dark-matter mass ratio similar to that inferred for systems of this mass (e.g. by Moster et al. 2010). The disc is, however, baryon-dominated within the central ~ 5 –10 kpc, and as such may develop spiral and bar instabilities.

For this galaxy model, our standard resolution has SPH smoothing lengths of ~ 5 –10 pc in the central few kpc of the disc. Our high-resolution simulations have ~ 2 –5 pc smoothing lengths and particle masses of $\sim 1000 M_{\odot}$, while the ultra-high-resolution simulations have particle masses of $100 M_{\odot}$ and 1 pc resolution in the bulk of the disc.¹⁰

High- z . This model is designed to approximate a massive, high-redshift and strongly unstable disc forming stars at a very high rate ~ 100 –400 $M_{\odot} \text{ yr}^{-1}$, typical of massive discs observed at $z \sim 2$ –4 (Erb et al. 2006; Genzel et al. 2008; Tacconi et al. 2010). The galaxy has a baryonic mass $1.7 \times 10^{11} M_{\odot}$, with $M_b = 7 \times 10^{10} M_{\odot}$ ($a = 1.2$ kpc), stellar disc $M_d = 3 \times 10^{10} M_{\odot}$ ($r_d = 1.6$ kpc), gas disc $M_g = 7 \times 10^{10} M_{\odot}$ ($r_g = 3.2$ kpc), initialized with stellar scaleheight 320 pc and $Q = 1$ in gas and stars. This gives a typical gas fraction of ~ 0.5 throughout the stellar and star-forming disc (with a larger H I gas reservoir at large radii). The halo has $M_{\text{halo}} = 1.44 \times 10^{12} M_{\odot}$ with $c = 3.5$ and a virial radius appropriate for that mass at $z = 2$. The system is baryon-dominated out to ~ 10 kpc. The spatial and mass resolution in these simulations are somewhat larger than in the Sbc simulation because of the larger total mass and spatial size of the disc; however, the Toomre mass and length-scale are also much larger, so this model is in a relative sense actually better resolved than the Sbc model.

MW. This system is initialized to represent a local, relatively gas-poor, MW-like disc. The galaxy has a baryonic mass of $7.13 \times 10^{10} M_{\odot}$, a bulge with $M_b = 1.5 \times 10^{10} M_{\odot}$, a stellar disc with $M_d = 4.73 \times 10^{10} M_{\odot}$ ($r_d = 3.0$ kpc) and a gas disc with $M_g = 0.9 \times 10^{10} M_{\odot}$ ($r_g = 6.0$ kpc). The disc gas fraction is $f_g = 0.05$ –0.10 throughout the disc out to ~ 8 kpc. The disc is initialized with a stellar scaleheight 300 pc and $Q = 1$. The halo has $M_{\text{halo}} = 1.5 \times 10^{12} M_{\odot}$, concentration $c = 12$ and R_{vir} appropriate for $z = 0$. Observations suggest that the MW hosts a pseudo-bulge or a bar instead of a classical bulge, so we initialize the bulge with a spherical exponential profile ($r_d = 1.0$ kpc), rather than a Hernquist (1990) profile, but since the bulge mass is small this makes little difference to our conclusions. At our ultra-high (high) resolution, the force and mass resolution in the gas are ≈ 2 pc (5 pc) and $200 M_{\odot}$ ($2000 M_{\odot}$).

Dwarf/SMC. This model is initialized to be similar to the inferred properties of the SMC (before entering the MW halo, at least; see Besla et al. 2010, and references therein), a typical low-mass, gas-rich dwarf. The galaxy has a baryonic mass $8.9 \times 10^8 M_{\odot}$, with a bulge having $M_b = 10^7 M_{\odot}$ ($a = 0.25$ kpc), a stellar disc with $M_d =$

$1.3 \times 10^8 M_{\odot}$ ($r_d = 0.7$ kpc) and gas disc with $M_g = 7.5 \times 10^8 M_{\odot}$ ($r_g = 2.1$ kpc). The disc is initialized with stellar scaleheight 140 pc and $Q = 1$. The halo has $M_{\text{halo}} = 2 \times 10^{10} M_{\odot}$, $c = 15$ and R_{vir} appropriate for $z = 0$. The system is dark-matter dominated at all radii outside of the central few hundred pc. For this model, our high-resolution simulations have a spatial resolution and particle mass of < 1 pc and $\sim 100 M_{\odot}$, respectively.

3 GLOBAL GALAXY PROPERTIES

The key simulations described in this paper are summarized in Tables 1 and 2. Table 1 summarizes the properties of each galaxy model. Table 2 summarizes the resolution of each simulation, the parameters of the star formation model and the key feedback parameters η_p and η_v (equations 5 and 7).

Fig. 1 shows face-on and edge-on images of the gas surface density distribution for simulations of each galaxy model with our fiducial parameter choices $\eta_p = \eta_v = 1$. Each image is shown in the quasi-steady feedback-regulated phase that sets in after a few dynamical times. The overall qualitative evolution is similar in all of the simulations with feedback. The gas cools efficiently to low temperatures and collapses by gravitational instability at the Jeans/Toomre scale. This leads to the formation of dense clumps that are the sites of star formation and, in our model, feedback. The resolved density contrast between the centres of star-forming clumps and the interclump medium is typically ~ 1000 but can be as high as $\sim 10^6$. The ISM sustains this clumpy structure as long as we evolve our simulations, as gas is blown out of individual clumps (by feedback) into the more diffuse ISM before being incorporated into new dense clouds. We defer a rigorous analysis of the lifetimes and evolution of individual clumps for future work (in preparation) analysing the properties of GMCs, where we can make rigorous comparisons with observations. But typically, we find average lifetimes of individual clouds $\lesssim 10$ Myr or a few free-fall times (weakly increasing with mass scale from the SMC through HiZ models), giving an integrated fraction ~ 1 –5 per cent of clump mass turned into stars.

This fragmentation is the natural extension of Jeans-mass GMCs in the MW and other nearby galaxies. Indeed, if we wish to explicitly resolve these scales, most of the gas mass *should* be in dense sub-clumps at something like the Jeans scale. The primary role of feedback is to regulate against runaway collapse and star formation in those clouds. Fig. 2 illustrates how these morphologies depend on the strength of feedback. We consider the HiZ case, which is most strongly unstable, at two different extremes (holding all details of the model fixed, except feedback strength). First, with feedback much stronger than is realistic, $\eta_p = 100$. In this case, essentially all sub-structure in the galaxy is ‘wiped out’, and the star formation is smoothly distributed over a ~ 10 kpc disc (despite < 10 pc resolution). This would be analogous to a MW model with no GMCs, where all star formation occurred in regions with local densities $\sim 1 \text{ cm}^{-3}$. Secondly, we consider a case with no feedback. In this extreme, the opposite occurs: the GMC complexes seen in Fig. 2 dissipate their internal velocity dispersions and experience runaway collapse and star formation. This collapse proceeds until the GMCs reach the simulation resolution limit and leads to all of the gas being at extremely high densities, $n \sim 10^6 \text{ cm}^{-3}$ (as we show explicitly below); a corollary is that the gas is converted into stars on essentially one (large-scale) dynamical time.

Fig. 3 shows the phase diagram for the gas in each of our fiducial simulations: we plot both the thermal sound speeds and turbulent velocities as a function of gas density (averaged over the smallest

¹⁰ The particular choice of gravitational softening is chosen as a compromise between matching the minimum SPH softening lengths, minimizing discreteness effects (see e.g. Power et al. 2003), and giving a similar maximum resolvable density in each simulation ($\sim 10^5 \text{ cm}^{-3}$) that is much larger than the mean GMC density but still below densities where processes of individual star formation and detailed thermal physics become dominant.

Table 2. Simulations plotted in this paper.

Simulation	N_{part}	SF law	η_p	η_v
HiZ_8.0_nofb	2e6	–	–	–
HiZ_8.2_nofb	2e7	–	–	–
HiZ_10.4	2e6	–	1.0	1.0
HiZ_8.10	2e6	–	2.0	2.0
HiZ_8.11	2e6	–	4.0	2.0
HiZ_9.1	2e6	–	10.0	1.0
HiZ_6.0_hr	1e7	–	1.0	1.0
HiZ_7.0_hr	6e7	–	1.0	1.0
HiZ_6.3_hr	1e7	$\dot{\rho} \propto \rho^{1.0}$	1.0	1.0
HiZ_6.4_hr	1e7	$\dot{\rho} \propto \rho^{2.0}$	1.0	1.0
HiZ_7.1_hr	6e7	$\epsilon = 0.35$ per cent	1.0	1.0
HiZ_7.2_hr	6e7	$\epsilon = 6.0$ per cent	1.0	1.0
HiZ_7.3_hr	6e7	$n_c = 2500$	1.0	1.0
HiZ_7.4_hr	6e7	$n_c = 25$	1.0	1.0
HiZ_10.4_hr	2e7	–	1.0	1.0
HiZ_10.5_hr	2e7	–	1.0	2.0
HiZ_10.6_hr	2e7	–	1.0	4.0
HiZ_10.7_hr	2e7	–	2.0	1.0
HiZ_10.8_hr	2e7	–	4.0	1.0
HiZ_10.9_hr	2e7	–	10.0	1.0
HiZ_10.14_hr	2e7	–	0.33	1.0
HiZ_10.11_hr	2e7	–	1.0	– ^a
HiZ_8.14_hr	2e7	–	4.0	2.0
HiZ_8.17_hr	2e7	–	5.0	4.0
HiZ_10.4_uhr	2e8	–	1.0	1.0
MW_8.3_nofb	3e6	–	–	–
MW_9.1	2e6	–	1.0	1.0
MW_10.7_hr	1e7	–	1.0	1.0
MW_10.8_hr	1e7	$\epsilon = 0.35$ per cent	1.0	1.0
MW_10.9_hr	1e7	$\epsilon = 6.0$ per cent	1.0	1.0
MW_10.10_hr	1e7	$\dot{\rho} \propto \rho^{1.1}$	1.0	1.0
MW_10.11_hr	1e7	$\dot{\rho} \propto \rho^{2.0}$	1.0	1.0
MW_10.12_hr	1e7	$n_c = 10$	1.0	1.0
MW_10.13_hr	1e7	$n_c = 1000$	1.0	1.0
MW_9.1_hr	2e7	–	1.0	1.0
MW_9.2_hr	2e7	–	1.0	– ^a
MW_9.3_hr	2e7	–	1.0	2.0
MW_9.4_hr	2e7	–	0.33	1.0
MW_9.5_hr	2e7	–	10.0	1.0
MW_8.4_hr	3e7	–	10.0	4.0
MW_8.5_hr	3e7	–	10.0	1.0
MW_10.2_hr	3e7	–	10.0	2.0
MW_10.4_hr	3e7	–	1.0	1.0
MW_9.1_uhr	2e8	–	1.0	1.0
MW_8_uhr	3e8	–	10.0	2.0
SMC_10.3_nofb	2e7	–	–	–
SMC_10.1_hr	2e7	–	4.0	2.0
SMC_10.2_hr	2e7	–	10.0	2.0
SMC_10.4_hr	2e7	–	1.0	1.0
SMC_10_uhr	1e9	–	10.0	2.0
Sbc_10.3_nofb	2e7	–	–	–
Sbc_10.1_hr	2e7	–	4.0	2.0
Sbc_10.2_hr	2e7	–	10.0	2.0
Sbc_10.4_hr	2e7	–	1.0	1.0
Sbc_10_uhr	2e8	–	10.0	2.0

Parameters of our key simulations (only simulations appearing in figures are listed; others are noted in the text):

(1) Name/ID. First characters correspond to the class of galaxy model ('SMC', 'MW', 'Sbc' or 'HiZ', as in Table 1).

(2) Total particle number.

(3) Star formation law. '–' corresponds to the default law: $\dot{\rho}_* = \epsilon \rho / t_{\text{ff}}(\rho)$ for $\rho > \rho_0$, with $\epsilon = 1.5$ per cent and $n_0 = 100 \text{ cm}^{-3}$; varied quantities are noted (see Fig. 6).

(4) Momentum-loading normalization η_p (see equation 5).

(5) Initial velocity normalization η_v (see equation 7).

^aAcceleration is continuous rather than discrete 'kicks.'

available scale, the SPH smoothing length). For low-density gas with $n \ll 1 \text{ cm}^{-3}$, the sound speed and turbulent velocity are often comparable, but for denser gas the turbulent velocity is always much larger than the thermal sound speed.

The characteristic densities of clumps/GMCs are evident in the peak of the gas distributions near $n \sim 100 \text{ cm}^{-3}$ in Fig. 3; the typical turbulent mach numbers for this gas are ~ 30 – 100 . Because of the high Mach numbers, turbulent motions rather than thermal motions are the dominant impediment to gravitational collapse. Specifically, the characteristic mass of large GMCs is set by the turbulent Jeans mass for the bulk of the matter, and corresponds to: $\sim 10^5 M_\odot$ in the SMC case, $\sim 10^6 M_\odot$ in the MW and Sbc cases, and $\sim 10^8 M_\odot$ in the HiZ case. These estimates agree reasonably well with the observed properties of massive cloud complexes in the respective systems. By contrast, if the gas were thermally supported, the characteristic mass of collapsed gas would be much smaller. For the dense gas, however, thermal support is only important on scales below the sonic length ($\lesssim 0.1 \text{ pc}$), which is well below our resolution limit.

The minimum pressure to prevent unresolved collapse below the resolution limit (equation 1) is well below the resolved turbulent pressure for the median densities in Fig. 3. This effective pressure does, however, produce the small 'upturn' in the turbulent δv at the very highest densities $n \gg 10^4 \text{ cm}^{-3}$. For our purposes, the key point is that we resolve the median GMC length, density and mass scales well, even in our lowest-resolution models.

3.1 Morphologies

There are a variety of morphologies present in the simulated galaxies depending on how self-gravitating the disc is. The high-redshift disc analogues (HiZ) are the most strongly self-gravitating and so fragment into very massive clumps ($M_{\text{Toomre}} \sim 10^8$ – $10^9 M_\odot$), which dominate the star formation. This morphology resembles the clumpy systems observed at $z \sim 2$ – 3 (Tacconi et al. 2006; Genzel et al. 2008; Law et al. 2009). This is even more clear when we focus on the region which contains half the star formation (middle panel) – this is dominated by a few giant complexes. Viewed edge-on, the HiZ model appears qualitatively similar to the 'clump chain/cluster' systems observed at high redshift.

The Sbc model fragments in a manner similar to that of the HiZ model. However, the disc is thinner, and the Jeans mass and length-scales are significantly smaller, so star formation is more distributed in many clouds [the number of massive clouds predicted at $Q \sim 1$ is $\sim (R/h)^2$ and is thus larger for thinner discs]. At slightly later times than that shown in Fig. 1, the system develops a strong stellar bar, and the gas – while still very clumpy – flows into the centre along the $m = 2$ mode. Flocculent spiral structure also develops in some of the Sbc runs at large radii.

The MW model in Fig. 1 shows clear grand design spiral structure. It is also weakly barred in the centre, though the bar feature is much more prominent in the stars. Note that this model has a lower gas fraction and is significantly more stable than the Sbc and HiZ models – the latter because it is dark matter or bulge dominated at all radii. As a result, the characteristic clump mass is smaller ($M_{\text{Toomre}} \sim 10^6 M_\odot$) and the Jeans length is much smaller relative to the effective radius (for a $Q \sim 1$ disc, $\lambda_{\text{Jeans}} \sim f_{\text{gas}}^2 R_e$, so ~ 100 times smaller here). As a result, the individual 'clumps' are much less prominent in the image, despite the fact that most of the mass in the star-forming disc does lie in thousands of resolved 'clouds' with masses $\sim 10^4$ – $10^6 M_\odot$. The small gas fraction also causes the disc to be significantly thinner in the edge-on image: $Q \sim 1$ implies $h \sim f_g R$ for weakly self-gravitating discs (e.g. Thompson, Quataert &

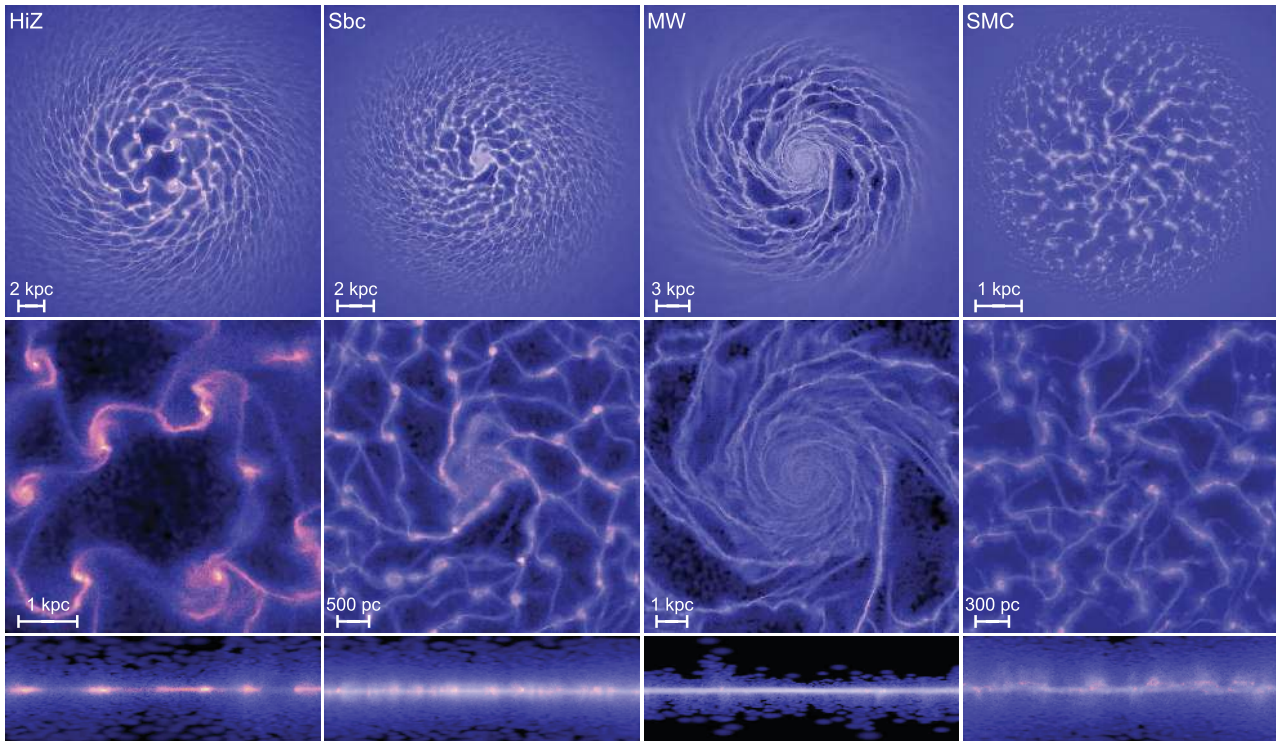


Figure 1. Images of the gas distribution for our fiducial simulations ($\eta_p = \eta_v = 1$) in the feedback-regulated quasi-steady state. Brightness shows the gas surface density while colour shows the specific SFR (increasing from blue to red); both are on a logarithmic scale spanning a dynamic range of $\sim 10^6$. Top: large scales (wide-field image) out to twice the half-gas mass radius. Middle: intermediate scales (zoom-in of the image at top) out to the half-SFR radius. Bottom: edge-on; scale is the same as the middle image. One example is shown for each of the initial conditions we model (HiZ_10_4_hr, Sbc_10_4_hr, MW_10_4_hr and SMC_10_4_hr in Table 2). The simulations develop complex substructure and exhibit a diverse range of gas morphologies. Most stars are formed in dense but resolved giant ‘molecular’ cloud complexes, which are the sites of the feedback modelled here.

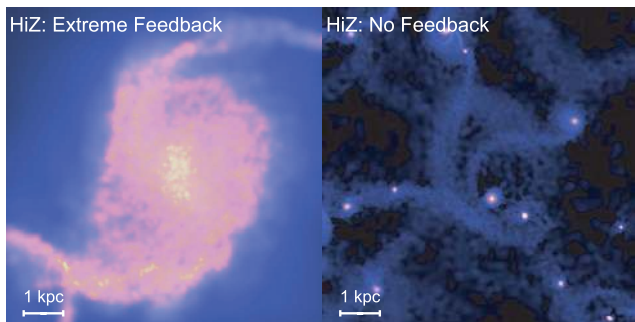


Figure 2. As Fig. 1 (middle left), but for an otherwise identical HiZ simulation with extremely strong feedback (left) with $\eta_p = 100$ (this is not a realistic choice but purely shown for illustrative purposes), and one with no feedback (right). With arbitrarily strong feedback, all collapse of gas into GMC complexes is suppressed. With no feedback, the cloud complexes in Fig. 1 undergo runaway collapse to the resolution limit (the single white pixels at right); the mass piles up at densities $\gtrsim 10^4$ times larger than in our ‘standard’ models.

Murray 2005). In future work (in preparation), we will investigate the detailed structural properties of the ISM and simulated GMC analogues to compare them to observations of the MW and Local Group galaxies.

The SMC-like model behaves quite differently from the MW model, although both are dark-matter dominated. The SMC model is completely stable to global instabilities and thus forms stars in a more uniformly distributed fashion. The ISM on these scales is

turbulent and patchy, with an irregular or (on large scales) featureless structure, typical of observed dwarf galaxies. Despite the low SFR of $\sim 0.1 M_\odot \text{ yr}^{-1}$, the turbulent velocities generated by stellar feedback are sufficient to make the system quite ‘puffy’ and thick (given the weaker potential depth). Fig. 1 shows that individual star-forming regions are resolved with size scales of < 10 pc.

Note that because the gas in this model is of quite low density, the cooling times are long and energy input via SNe and stellar winds will have a significant effect on the gas morphology. There are plain indications here that the present model, including momentum from radiation pressure alone, is not a complete description of the ISM. For example, the temperature of the ‘diffuse’ ISM in *all* the galaxy models tends to be much too low. We show this explicitly in Fig. 3, where we plot the phase distribution of the gas. The volume-filling gas distributed between dense clouds is almost entirely ‘warm’ ($10^4 \lesssim T \lesssim 10^5$ K), with negligible mass in the characteristic ‘hot phase’ of the ISM at $T \gtrsim 10^6$ K (there is some, generated by shocks, in the stronger HiZ and Sbc cases, but even here it is less than a per cent of the total gas mass). Some additional heating mechanisms, such as SNe and ‘fast’ stellar winds, are probably critical to explain the full temperature structure of the ISM. In future work we will investigate this in detail, with explicit models for various heating terms; for now, we simply note that the small mass fraction in the ‘hot’ phase, while potentially important for phenomena such as galactic winds, is unlikely to change the structure of cold regions as it contains little mass and, even in MW-like galaxies, contributes only ~ 10 per cent to the typical ISM pressure (Boulares & Cox 1990). We see in Fig. 3 that the turbulent velocities are much larger in all dense gas than the thermal sound speeds (and tend to be

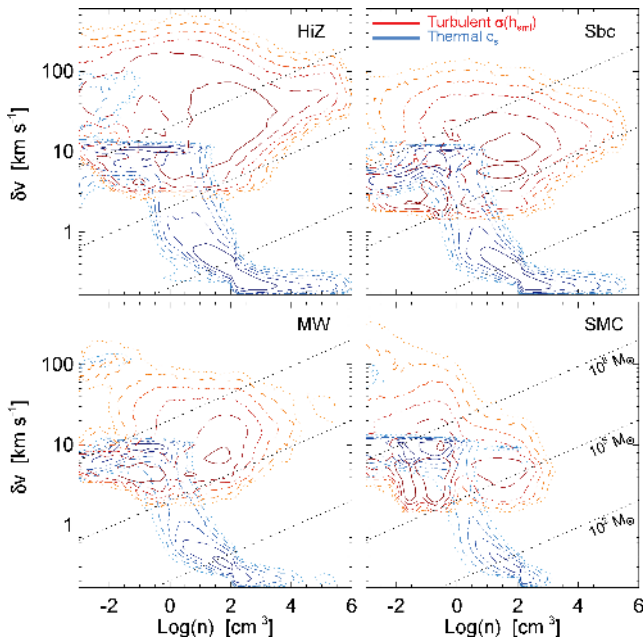


Figure 3. Phase diagram for the gas in the fiducial simulations in Fig. 1, at times in the feedback-regulated quasi-steady state. Contours are iso-density at $\sim 10^{-3}, -2.5, -2, -1.5, -1, -0.5$ of maximum (progressively darker dotted, short-dash, dot-dash, dot-dot-dot-dash, long-dash, solid contours, respectively). Blue contours show the thermal sound speeds $c_s \propto T^{1/2}$; red contours the local turbulent velocity dispersion σ (averaged within one gas smoothing length h_{smf} around each particle). Lines of constant Jeans mass $\propto \delta v^3 n^{-1/2}$ (black dotted) are shown for comparison. The median clump/cloud gas density is evident in the peak near $\sim 100 \text{ cm}^{-3}$. For all the dense gas, the thermal pressure is negligible compared to the turbulent pressure/velocities. As a result, the turbulent Jeans mass governs large-scale collapse and corresponds to the mass of massive clumps/GMCs (from $\sim 10^5 M_\odot$ in the SMC model through $\sim 10^8 M_\odot$ in the HiZ model); these are very well-resolved. The thermal Jeans masses are much smaller, but are only relevant for the dynamics on scales below the sonic length ($< 0.1 \text{ pc}$) where individual groups of stars form; this is unresolved, hence the necessity of an ‘effective’ small-scale star formation law. The slight ‘upturn’ in $\sigma(h_{\text{smf}})$ at $n \gg 10^4 \text{ cm}^{-3}$ (most evident in the HiZ model) comes from the minimum pressure corresponding to the Truelove et al. (1997) Jeans condition (equation 1). This indicates where resolution limits prevent us from following further collapse to higher densities.

near-virial), making the detailed thermal structure sub-dominant on these scales.

3.2 Star formation histories

Fig. 4 shows the star formation history (SFH; galaxy-integrated SFR as a function of time) of each of our galaxy models for the same feedback parameters used in Fig. 1; we also compare to simulations of the same galaxy models that include cooling and star formation, but not stellar feedback.

In the models without feedback, the SFR increases to a peak value on a single global dynamical time; the SFR remains at this value until the gas in the disc is exhausted. The peak SFRs in the simulations without feedback are a factor of $\gtrsim 10$ larger than those observed in the systems that motivate these galaxy models – the observed values are $\sim (50\text{--}300, 3\text{--}20, 2\text{--}4, 0.1\text{--}0.5) M_\odot \text{ yr}^{-1}$ for high- z non-merging SMGs (Forster Schreiber et al. 2009), low- z non-merging LIRGs (Sanders & Mirabel 1996), the MW and similar-mass spirals at $z = 0$, and isolated SMC-mass systems at $z = 0$ (Noeske et al. 2007;

Salim et al. 2007). In Section 5, we explicitly show that these models also lie well off of the observed KS relation between SFR and gas surface density. Physically, this is because in all of our simulations the gas can cool to an arbitrarily low temperature on a time-scale shorter compared to the local dynamical time. In the absence of feedback, the gas is then violently unstable to runaway clumping and rapid star formation. The net result is that $\dot{M}_* \sim M_{\text{gas}}/t_{\text{dyn}}$, i.e. most of the gas is converted into stars on a single dynamical time, the time-scale for the initially thermally supported gas disc to collapse. This behaviour is physically correct in the absence of stellar feedback, and should be recovered in any simulation that does not include such feedback.

A number of authors have suggested that instabilities due to self-gravity alone might generate the turbulence needed to slow down star formation in galaxies (e.g. Ballesteros-Paredes et al. 2007; Tasker & Tan 2009; Krumholz & Burkert 2010). Fig. 4 is not consistent with this hypothesis. Absent stellar feedback, the majority of the gas accumulates into dense clumps in which star formation proceeds unimpeded. Independent simulations at similar resolution but with different physics included have reached the same conclusion (e.g. Bournaud et al. 2010). We thus find that stellar feedback is critical to regulating star formation in galaxies. A more subtle question is, when strong feedback is present, does it ‘drive’ the turbulence, or is it still primarily driven by gravity? We will investigate this more quantitatively in future work. It generally appears, however, that the role of feedback is to offset the dissipation of turbulence and relative motions (particularly in dense regions), so in this sense it ‘provides’ momentum; but the level it must provide, and the turbulent cascade and regulation of those motions, is primarily dictated by gravity.

In contrast to the models without feedback, our simulations with stellar feedback rapidly reach a maximum SFR and then remain at this quasi-steady state for many dynamical times. In some of our simulations, there is a slow increase in the SFR on a time-scale longer than the disc’s dynamical time; this is a consequence of both slowly growing secular instabilities (e.g. halo bars) and spatial redistribution of gas by the stellar feedback (e.g. gas being driven in fountains from small to large radii). Eventually, however, since these are isolated systems without continuous gas accretion, the SFR must decline by gas exhaustion, but this decline is much more gradual than in the absence of feedback. Test runs, run for ~ 5 times longer, confirm that there is no new behaviour after the first few dynamical times; the SFRs gradually decline as gas is exhausted. In Section 5 we show that our simulations with stellar feedback are reasonably consistent with the observed KS relation. This is true for a range of feedback parameters. Below we discuss the physical origin of this low star formation efficiency.

3.3 Structural properties

Fig. 5 shows a number of the properties of the ISM in our HiZ model as a function of time and radius: the vertical velocity dispersion (σ_z : thermal and turbulent), the Toomre Q parameter¹¹ of the gas, the mass-weighted density distribution function, the total momentum supplied to the gas, the ‘kick’ velocity particles initially receive and the (momentum-weighted) optical depth of gas clumps where the kicks are applied (i.e. the optical depth for the regions where

¹¹ We define Q here as $\sigma \kappa / \pi G \Sigma_{\text{gas}}$, where σ is the full gas velocity dispersion, κ is measured from the azimuthally averaged mass profile and Σ_{gas} is the gas surface density.

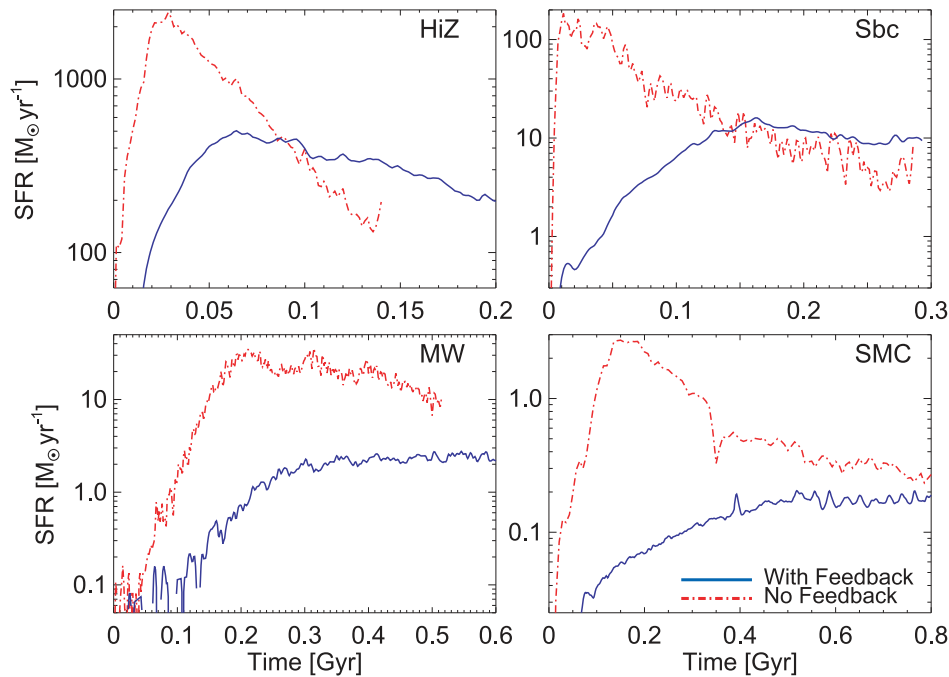


Figure 4. Total SFR for each of our galaxy models in Table 1 as a function of time, both with feedback ($\eta_p = \eta_v = 1$) and without. The time-scales are different in each model and correspond to the characteristic dynamical time-scales in each system (longer in the more stable, dark-matter-dominated systems; see Table 1). Absent feedback (red dot-dashed line) the gas collapses on a dynamical time, leading to an SFR well in excess of that observed in similar systems; the SFR then declines as the gas is exhausted. With stellar feedback, the SFR reaches an approximate equilibrium in which feedback maintains marginal stability to gravitational collapse ($Q \sim 1$).

most of the feedback occurs). These results provide a more quantitative view of the quasi-steady feedback-regulated state reached in our simulations. We show the results for the HiZ model because the strong gravitational instability, high gas fraction and very high SFR make it the model most sensitive to variations in our feedback prescription and give the largest differences between models with and without feedback. However, we find identical qualitative conclusions (discussed below), modulo the absolute value of the various quantities, for each of our other galaxy models. We focus on three different simulations in Fig. 5. The first is one of our ultra-high-resolution runs (*HiZ_10_4_uhr*) with $\eta_p = \eta_v = 1$ and 2×10^8 particles, in which a typical Jeans-mass clump in the disc is resolved with as many as $\sim 10^5$ particles. We compare this to a lower resolution simulation with the same feedback parameters (*HiZ_10_4*) and to a lower resolution simulation which has $\eta_p = 10$ (*HiZ_9_1*) to compensate for the poorer resolution of the densest star-forming regions.

Perhaps the most important result in Fig. 5 is that the ISM properties do not depend sensitively on either resolution or the momentum feedback parameter η_p (the SFH does depend mildly on η_p as we show in Section 4.2). The key reason for this is that the disc always self-regulates to maintain

$$Q \simeq \frac{\delta v \Omega}{\pi G \Sigma_g} \sim 1, \quad (10)$$

where δv is the turbulent velocity dispersion induced by the stellar feedback. Fig. 5 shows explicitly that all of the simulations maintain $Q \sim 1$ in the feedback-regulated phase (top-middle panel). The differences between models are small and all within the range of random variations and noise. Fig. 5 also shows the (mass-weighted) vertical velocity dispersion $\sigma_z = \sqrt{c_s^2 + \delta v_z^2}$ of the gas as a function of time (top-left panel). Initially σ_z decreases rapidly as the thermal

support is radiated away. As star formation commences, however, stellar feedback quickly drives the turbulent velocity to $\delta v_z \sim 30\text{--}50 \text{ km s}^{-1}$. Given this turbulent velocity, the vertical scaleheight of the disc is a few hundred pc, with only a modest dependence on radius; at all radii this thickness is much larger than the resolution limit.

The early-time and late-time values of σ_z in Fig. 5 are comparable because in both limits $Q \sim 1$. The models are initialized with thermal support and $Q = 1$ but this is quickly replaced by turbulent support that self-consistently maintains $Q \sim 1$ at later times. The velocity dispersions in Fig. 5 are also in reasonable agreement with the observed values in high-redshift discs (Förster Schreiber et al. 2006). The other galaxy models also self-regulate at $Q \sim 1$. However, given their lower masses, gas fractions and SFRs, this translates to lower absolute velocity dispersions: $\delta v \sim 10 \text{ km s}^{-1}$ in the MW and Sbc models, and $\approx 6 \text{ km s}^{-1}$ in the SMC model (modulo rescaling by this absolute value; however, the dependence of σ_z on time, resolution and η_p is nearly identical to that shown in Fig. 5).

The top-right panel in Fig. 5 shows the mass-weighted gas density distribution averaged over the entire galaxy once the star formation reaches an approximate steady-state (since most of the gas mass is near $\sim 3 \text{ kpc}$, the density distribution in an annulus at this radius is quite similar); the distribution is close to lognormal (LN) in all of the simulations with a median density of $\sim 100 \text{ cm}^{-3}$ and a broad dispersion of $\sim 1.5 \text{ dex}$. The highest resolved densities reach $> 10^6 \text{ cm}^{-3}$ in the ultra-high-resolution simulation, but it is important to note that gas does not simply ‘pile up’ gas at these high densities, which it does if we do not include feedback. We show this explicitly in Fig. 5 by including the density PDF for a simulation with identical initial conditions, but no feedback (see also the density distributions in the simulations without momentum-feedback in Teyssier et al. 2010) – in this case almost all the gas ends up at

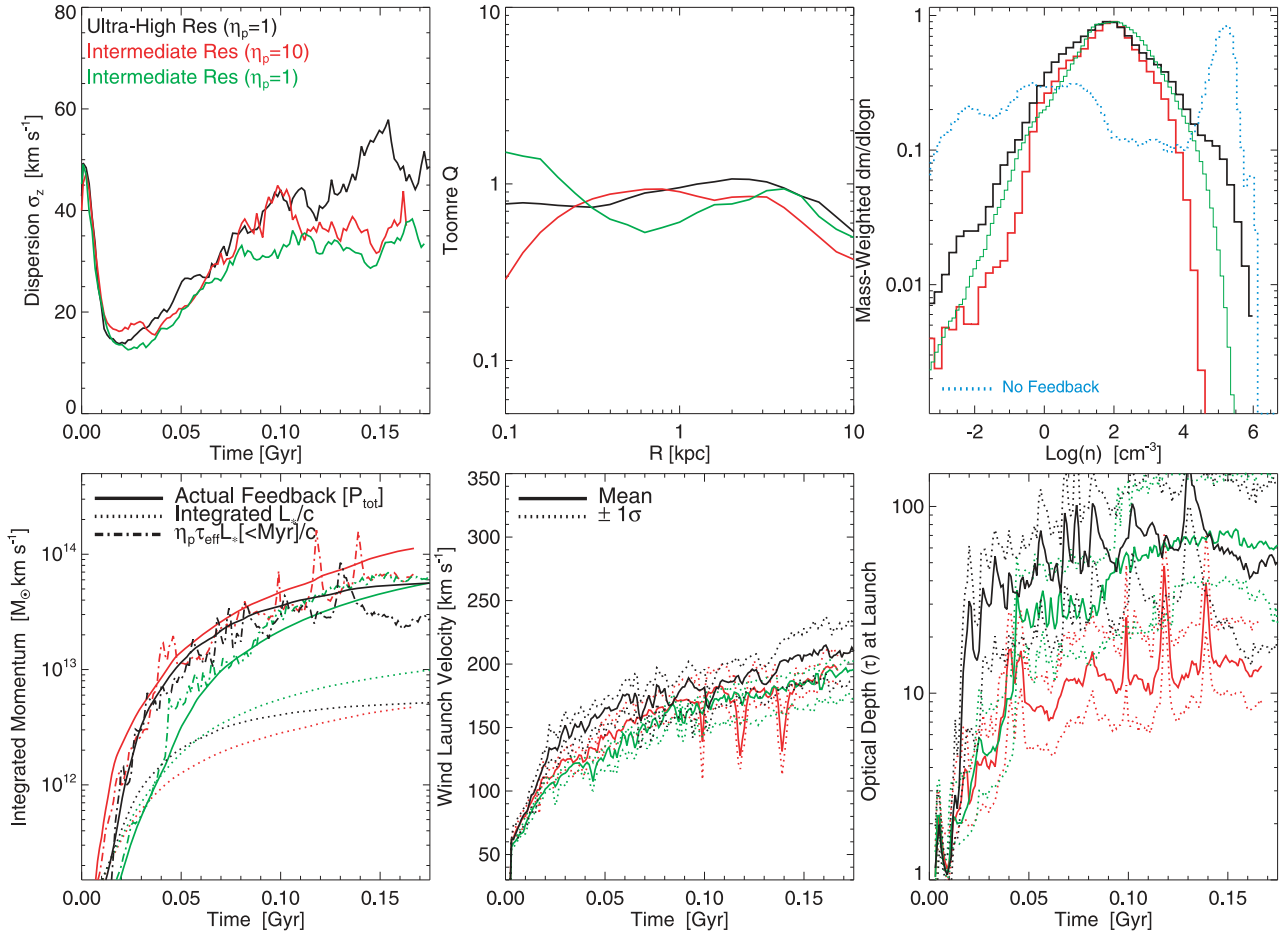


Figure 5. Properties of the ISM and feedback in several of our HiZ simulations: intermediate (HiZ_10_4) and ultra-high-resolution (HiZ_10_4_uhr) simulations with $\eta_p = 1$ and $\eta_v = 1$, and an intermediate-resolution (HiZ_9_1) simulation with $\eta_p = 10$ (see Table 2). Top left: vertical gas velocity dispersion, $\sigma_z = \sqrt{c_s^2 + \delta v^2}$ (averaged over the entire disc, weighted by gas mass). The initial disc is thermally supported, but this thermal energy is rapidly radiated away; at later times a comparable σ_z is produced by feedback-driven turbulence. Top centre: gas Toomre Q parameter in narrow radial annuli as a function of radius (averaged over times > 60 Myr, when the system is quasi-steady state). Top right: gas density distribution (gas mass per interval in $\log n$) is LN with $\sim 1 - 1.5$ dex dispersion; low- and high-resolution simulations converge to the same median density, but at low resolution the full width is not resolved. With no feedback (dotted), the gas piles up at the highest resolvable densities. Bottom left: sum of all momentum ($|\Delta p|$) injected via feedback (solid; equation 5) compared with input optical-UV stellar photon momentum $= \int L_* c^{-1} dt$ (dotted). Note that the momentum injected is nearly the same for all three simulations, including $\eta_p = 1$ and $\eta_p = 10$. The dot-dashed line shows that the input momentum is well-reproduced using the optical depths from the bottom-right panel and only the very young stars ($< 10^6$ yr old). This demonstrates that star-forming clusters disrupt rapidly. Bottom centre: mean ‘kick’ velocity given to gas particles at their launching from young stellar clusters (and 1σ dispersion); values approach $\sim 150\text{--}200$ km s $^{-1}$, as expected given the massive $10^8 M_\odot$ clumps forming in these simulations. The kick velocity is much larger than the actual dispersion in the disc because the particles shock and share their momentum immediately. Bottom right: resolved IR optical depths of gas clumps used in the feedback model (equation 5). In the simulations with $\eta_p = 1$, $\tau \sim 30\text{--}50$, corresponding to $\Sigma \sim 10$ g cm $^{-2}$, comparable to the observed surface densities of star clusters on \sim pc scales. The simulation with $\eta_p = 10$ has the same total input momentum (bottom-left panel) but as a result the gas clumps only collapse to $\tau \sim 10$. A comparison of our MW-like models gives identical qualitative conclusions, but with systematically shifted absolute values: $\sigma_z \sim 10$ km s $^{-1}$, $Q \approx 1$, $\langle n \rangle \sim 1$ cm $^{-3}$, ‘kick’ $v \sim 30\text{--}50$ km s $^{-1}$ and $\langle \tau \rangle \sim 10\text{--}30$ at $\eta_p = 1$.

the maximum density allowed by our resolution ($\sim 10^6$ cm $^{-3}$), with a small tail at low densities. With feedback included, however, most of the mass is in GMC-like structures, but within those structures feedback ensures that most of the mass is in a more diffuse phase, rather than in the densest star-forming cores. The same conclusions pertain to our other galaxy models, but with lower median densities as expected; the volume-averaged $\langle n \rangle \sim 1$ cm $^{-3}$ in the MW and Sbc models, with much of the mass in the star-forming disc in GMCs with a mean $\langle n \rangle \sim 10\text{--}30$ cm $^{-3}$ (and a resolved tail up to $\sim 10^6$ cm $^{-3}$). We caution that the distribution of low-density gas ($n \ll 1$ cm $^{-3}$) can be strongly altered by other sources of energetic feedback, such as SNe, stellar winds and photo-ionization; the most

dense gas, however, is where radiation pressure is likely to be most important.

The bottom panels in Fig. 5 quantify the magnitude of the stellar feedback: we show the integrated momentum supplied to the gas as a function of time, the typical initial velocity of the kicks as they are imparted to particles at the star-cluster scale and the momentum-weighted optical depth of the gas clumps where the feedback is applied.

The values of the ‘initial’ kick velocities given to the particles are large for the HiZ model, but not surprising given the very large star cluster masses ($\sim 10^8 M_\odot$) associated with the giant clumps in gas-rich high-redshift systems (see Murray et al. 2010; Genzel

et al. 2011); by contrast, the initial kicks in the MW-like system are much lower, tens of km s^{-1} . Note also that the initial kick velocities are much larger than the velocity dispersion in the galaxy (in both cases): this occurs because the particles immediately interact with the surrounding ISM and share their momentum. In Section 4.2 we show that for this reason, the choice of the initial kick velocity – or even whether to continuously accelerate rather than ‘kick’ particles – is largely irrelevant.¹² Instead, the important parameter is the total momentum supplied to the gas.

With the large SFR and reasonably large kick velocities of the HiZ model, we might expect a sizeable super-wind to be generated by this feedback mechanism alone. However, in fact, the amount of mass in a proper super-wind (defined as e.g. the mass flux at $>V_c$ escaping to at least ~ 20 kpc) is relatively small relative to the SFR, about ~ 10 per cent. This is because, as described above, the momentum is coupled in extremely dense regions and so rapidly shared among the gas particles. This can maintain a large velocity dispersion in the disc, but will not efficiently launch gas well out of the disc. Occasionally some material has an un-obstructed sightline out of the disc and escapes, but even then, the launch velocities are typically below the circular velocity, so the material is lofted up above the disc and then returns rapidly. It is likely that rather than winds being launched directly out of the galaxy from individual star clusters, some continuous acceleration mechanism is needed to act on gas once this local mechanism pushes it above the disc, in order to accelerate it out of the galaxy halo. This could be either pressure acceleration from hot, SNe-heated gas, or continuous radiation acceleration from the light which escapes the dense, optically thick regions we model here. In future work, we will investigate the properties of the galactic super-winds in more detail, and examine how these mechanisms interact with the feedback mechanism described here.

Fig. 5 shows that the total momentum supplied to the gas is significantly larger than $\int (L/c) dt = E_{\text{rad}}/c$ because of the non-zero optical depths (where E_{rad} is the total radiated energy). In fact, the numerical results are consistent with the total momentum supplied being given by $\simeq \eta_p \langle \tau_{\text{IR}} \rangle E_{\text{rad, young}}/c$, where $E_{\text{rad, young}}$ is the integrated luminosity from young stars with ages $< 10^6$ yr. This is because the feedback begins to disperse the densest regions on a $\sim 10^6$ yr timescale. Fig. 5 also shows the median and dispersion in the clump optical depths for the regions where the feedback is applied: $\tau_{\text{IR}} \sim 50$ in the highest resolution simulation. This corresponds to gas surface densities $\sim 10 \text{ g cm}^{-2}$, similar to the observed surface densities of massive star clusters. The average τ over the entire disc is, of course, significantly smaller, $\tau_{\text{IR}} \sim 0.1$ – 1 . For this reason, for the MW, Sbc and SMC models, although the disc-averaged τ_{IR} is significantly smaller than the HiZ model, their ‘effective’ τ_{IR} is not too much smaller. Despite the global gas mass being lower, the mass that actually forms stars and star clusters tends to be compact cores at high three-dimensional ($n \gtrsim 10^4 \text{ cm}^{-3}$) and surface densities ($\Sigma \gg 1000 \text{ M}_\odot \text{ pc}^{-2}$).

Fig. 5 shows that the total momentum input does not depend that strongly on resolution or on η_p at a given resolution. In fact, the optical depths decrease with increasing η_p , maintaining approximately the same total momentum input. Physically, this is because for more/less efficient feedback the gas collapses to lower/higher densities (on average). The fact is that the total momentum supplied by feedback depends only weakly on resolution and η_p is a

consequence of the disc self-regulating to maintain $Q \sim 1$. This constraint picks out a δv as a function of Σ_g and Ω (equation 10) – the momentum input then adjusts to produce the required δv . Again, the same is true in all galaxy models.

The column density distribution within individual star-forming clumps can strongly influence the efficacy of radiation pressure feedback. For example, if there is a very broad distribution with a large number of optically thin sightlines, then even though the average column density of a clump in the IR may be large, a sizeable fraction of photons would leak out of optically thin sightlines and the effective optical depth for the purposes of feedback would be reduced ($\eta_p < 1$, in our parametrization). To quantify this, we considered a number of massive clumps in our HiZ simulation and determined the optical depth along ~ 1000 sightlines evenly spaced in solid angle from the clump centre outwards (following the methodology in Hopkins et al. 2005). The characteristic dispersion in optical depth for a given clump is small, ~ 0.2 dex, similar to what has been found in smaller-scale simulations of individual clouds (Ostriker, Stone & Gammie 2001) and measured observationally (Wong et al. 2008; Goodman, Pineda & Schnee 2009).¹³ Note that this dispersion for an individual star-forming clump is much smaller than for the galaxy as a whole. A key consequence of the relatively narrow column density distribution within clumps is that only a negligible fraction of the sightlines are optically thin enough for the photons to rapidly leak out; it thus appears reasonable to use the mean clump column density when quantifying the feedback produced by the IR radiation (as we assume in our fiducial models; see Section 2.2.2).

It is also straightforward to calculate the total momentum deposition or infer it from the momentum coupled and typical velocities, $\dot{E}_w \approx (1/2) \dot{p}_w v_w$. For the values in Fig. 5, this is about 0.2–0.4 per cent of the stellar luminosity. Interestingly, recent observations of massive stars (Freyer, Hensler & Yorke 2006) and star-forming regions (Lopez et al. 2011) have suggested similar ~ 1 per cent efficiencies for transfer of luminous energy into bulk motions and (post-shock) thermal energy.

In future work (in preparation), we will compare the structural properties of the ISM and dense gas in these simulations and local observed galaxies in detail. However, in low-density gas, typical of much of the mass in the SMC model and the intermediate/diffuse phases in the Sbc and MW models, it is likely that other processes (shock heating by SNe and stellar winds, photo-ionization, magnetic fields) can play a significant role in shaping the gas dispersions and density distribution. We therefore defer a more detailed comparison with these observations until the models include some of these effects. However, preliminary experiments show that while the systematic values discussed above can shift, the qualitative conclusions remain intact as other feedback mechanisms are introduced.

4 DEPENDENCE ON MODEL PARAMETERS

In this section we show that the results summarized in Section 3 do not depend sensitively on the assumed local star formation law (Section 4.1) or the precise feedback parameters adopted (Section 4.2). We focus on the SFH when presenting these results. We again focus on the HiZ model since it is the most self-gravitating and therefore

¹² For the same reason, the total fraction of gas particles initially ‘kicked’, which in these models is about ~ 10 per cent, is unimportant.

¹³ In detail, we find there is a narrow core in the distribution and a broader-than-LN wing; the distribution is better fit by an exponential at high columns, with $P(\log N_H) \propto \exp[-|\log N_H/N_0|/0.22]$. This is broadly consistent with randomly distributed ‘patchy’ obscuration within clouds.

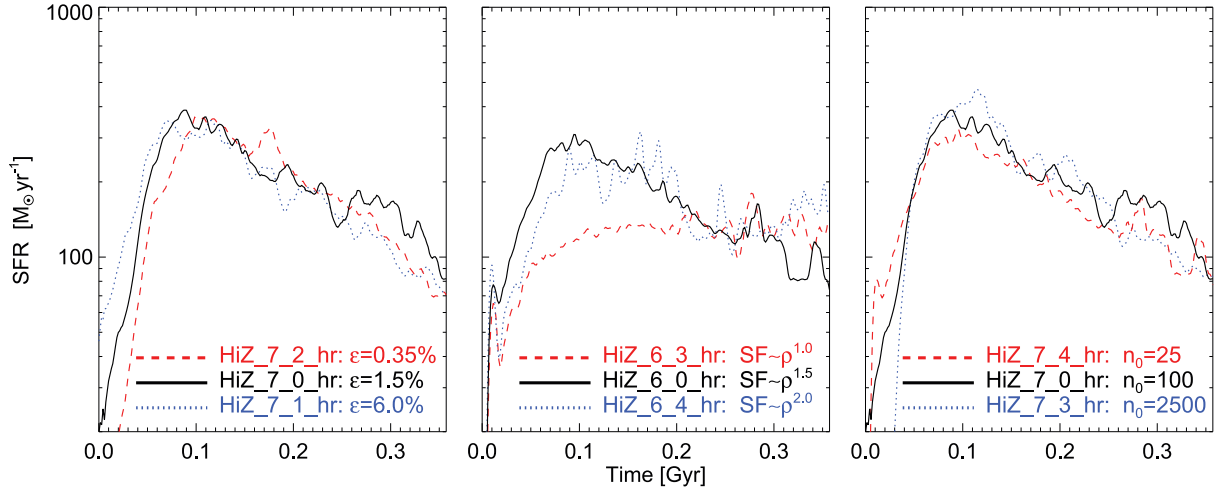


Figure 6. SFR as a function of time for the HiZ model for variations in the *small-scale* (high-density) star formation law; all runs use our fiducial feedback parameters ($\eta_p = \eta_v = 1$). These results demonstrate that the global SFR depends only weakly on the small-scale star formation law. In each panel, the black solid line shows the standard star formation model: $\dot{\rho}_* = \epsilon \rho / t_{\text{ff}}$ above a threshold density $n_0 = 100 \text{ cm}^{-3}$, with $\epsilon = 0.015$ and $t_{\text{ff}} = \sqrt{3\pi/32} G \bar{\rho} \propto \rho^{-0.5}$. Left: variations in the star formation efficiency ϵ . Middle: variations in the density PL of the star formation model: $\dot{\rho}_* \propto \rho^n$ with $n = 1, 1.5, 2$, normalized so that $\dot{\rho}_*$ is the same as the default model at n_0 . Right: variations in the threshold density for star formation n_0 .

its SFH tends to be the most sensitive to variations in the simulation parameters. However, we carried out the same experiments for the MW-like simulation and found comparable results, which are also shown below. In the Appendix we show that our results also do not depend strongly on how we numerically implement the stellar feedback.

4.1 Dependence on the local SF law

Figs 6–7 show how the SFH in feedback-regulated simulations depends on the *local* star formation prescription used at high densities. For our fiducial $\eta_p = \eta_v = 1$ model, Figs 6–7 vary the star formation efficiency in dense gas ϵ , the power-law (PL) slope of the star formation law and the threshold density for star formation n_0 (equation 2).

The key result in Figs 6–7 is that there is very little dependence of the SFH on the high-density star formation law. Specifically, Fig. 6 (left-hand panel) shows results for our canonical value of $\epsilon = 1.5$ per cent, a larger value of 6 per cent and a smaller value of $\epsilon = 0.35$ per cent (we have also examined several intermediate values). This range of ϵ corresponds to a factor of 20 different star formation time-scale at a fixed density. We find, however, at most ~ 30 per cent differences in the SFR once the system has reached approximate equilibrium. In the MW-like model (Fig. 7), the conclusion is identical. Secondly, we vary the PL index of the local SF law (middle

panel). In our canonical implementation, $\dot{\rho}_* \propto \rho / t_{\text{dyn}} \propto \rho^{1.5}$; we compare this to simulations with $\dot{\rho}_* \propto \rho / t_0 \propto \rho^{1.0}$ and $\dot{\rho}_* \propto \rho^{2.0}$, normalized such that $\dot{\rho}_*$ is identical at the threshold density ρ_0 . There are early-time differences in the star formation histories, but given the magnitude of the change to the star formation prescription the results are broadly similar. The biggest change appears when $\dot{\rho}_* \propto \rho$, i.e. when the gas consumption time-scale is constant, independent of density; in this regime, the gas cannot necessarily be consumed quickly on small scales, so the collapse from large to small scales is no longer the dominant rate-limiting step in star formation (a slightly larger exponent, e.g. $\dot{\rho}_* \propto \rho^{1.2}$, much more closely resembles the canonical $\propto \rho^{1.5}$ case). We show this for the MW-like model in Fig. 7, comparing $\dot{\rho}_* \propto \rho^{1.5}$, $\dot{\rho}_* \propto \rho^{2.0}$, $\dot{\rho}_* \propto \rho^{1.1}$. The relative differences in the $\dot{\rho}_* \propto \rho^{2.0}$ are even smaller, and making the exponent just slightly super-linear ($\propto \rho^{1.1}$) gives a nearly identical SFR to $\propto \rho^{1.5}$. Finally, we vary the SF density threshold n_0 (right-hand panel); from our canonical value of 100 cm^{-3} , we also consider $n_0 = 25 \text{ cm}^{-3}$ and $n_0 = 2500 \text{ cm}^{-3}$ (with other intermediate values sampled as well). At early times, before the initial conditions have been replaced by a self-consistent equilibrium, the SFR is higher with a lower threshold (unsurprisingly). However, once enough time has elapsed for gas to collapse to high densities and initiate significant feedback, the SFHs are again nearly identical despite a factor of 16 change in the threshold for star formation. The same result obtains in the MW model, for which (given the lower mean density) we vary $n_0 = 10\text{--}1000$. Moreover, for a MW-like model with similar resolution, Saitoh et al. (2008) find the same result in a more limited study varying the small-scale star formation efficiency, but with a different simulation algorithm and different feedback mechanism (SNe) implemented. We have also repeated these experiments for different values of η_p ($=1/3, 4, 10$) and η_v ($=2$ and continuous acceleration), and reach similar conclusions in each case.

Our interpretation is that the weak dependence of the global SFR on the small-scale star formation model is a consequence of the turbulence driven by stellar feedback, and the self-regulation to $Q \sim 1$ (see e.g. Thompson et al. 2005). Specifically, gravity causes gas to collapse to high density, where some of it forms stars, while most

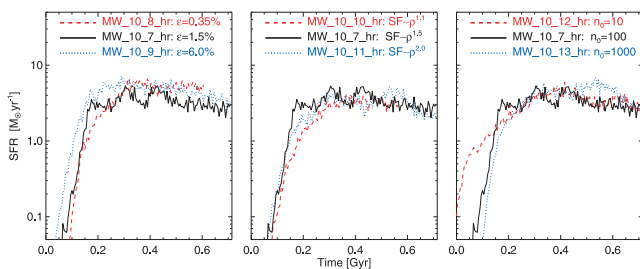


Figure 7. As Fig. 6, but for the MW model. Again the global SFR is independent of the local, high-density SF law.

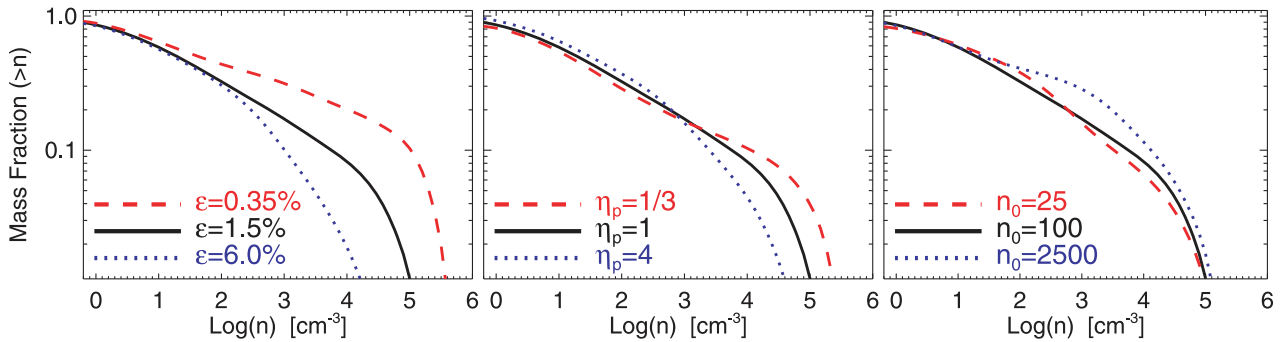


Figure 8. Cumulative gas mass fraction above a given density n for the (high-resolution) HiZ model for variations in the small-scale star formation law (Fig. 6) and feedback efficiency (Fig. 9). Left: density distribution for different values of the star formation efficiency ϵ : for smaller (larger) ϵ , more (less) mass must collapse to high densities for the star formation to self-regulate (the high- ρ cut-off is set by resolution limits). Middle: density distribution for different values of the momentum deposition per unit star formation (η_p ; equation 5). For larger η_p , gas is more efficiently removed from dense regions. Right: density distribution for different values of the threshold density for star formation n_0 . Larger n_0 requires that the gas should collapse to somewhat higher densities before the star formation can self-regulate.

of the gas is driven back out to lower densities by feedback. The key step that regulates the SFR is this cycle of collapse and expulsion, which has a time-scale \sim the global dynamical time of the galaxy – this is also the decay time-scale for large-scale turbulence in the galaxy. The details of feedback on small scales should also not be important, so long as it is sufficient to self-regulate (compare our result to Saitoh et al. 2008). So long as the star formation time-scale at the threshold density is small compared to the global dynamical time (i.e. ϵ not too small and $\rho_0 >$ the $\langle \rho \rangle$ of the galaxy) and the threshold is well-resolved numerically (i.e. ρ_0 is not too large), the SFR is insensitive to the details of the small-scale star formation law.

More generally, if the support needed to maintain stability against runaway star formation is set by the luminosity/mass in young stars, the SFR can self-regulate to $Q \sim 1$. For example, if the SFR set by the small-scale physics is too low to maintain $Q \sim 1$ given the large-scale conditions, gas simply collapses further to slightly higher densities until the required feedback power is generated, sufficient to halt further collapse. The high-density star formation law thus determines some of the properties of the high-density gas, but not the global SFR.

Fig. 8 supports this interpretation by showing the cumulative gas density distribution (mass fraction $>n$) for different values of ϵ (left-hand panel), n_0 (right-hand panel) and the feedback parameter η_p discussed in the next section (middle panel). Fig. 8 shows that when the high-density star formation efficiency ϵ is smaller (larger), the gas distribution adjusts so that there is more (less) mass at high densities, so as to produce a similar total SFR (as in Fig. 6.) When the threshold density n_0 is varied, the mass at high densities shifts accordingly. For example, increasing n_0 causes the gas that would have formed stars at the previous threshold to collapse to somewhat higher densities before it begins to form stars.

Note that the mass at low densities is nearly unchanged – the discs are not in global collapse (they are regulated by feedback), but the gas locally collapses to the densities needed to maintain the same SFR. For this reason, the Schmidt law predicted by each of the models in Fig. 6 is nearly identical. They have the same range in surface densities (set by the initial conditions and exhaustion via star formation, which must be the same since they have the same SFH), and so self-regulate at the same SFR.

Schaye et al. (2010), using much lower resolution cosmological simulations, also find a galaxy wide SFR that is independent of

the details of the small-scale star formation law employed. However, in their case, because star formation laws are applied globally (on $>kpc$ scales), it is the global gas mass that self-adjusts (e.g. lowering the star formation efficiency leads to inflows larger than the SFR building up the global gas mass until the SFR is similar to the cosmological inflow rate), so the systems do not necessarily obey the observed Schmidt–Kennicutt relation. In our case, neither the SFR nor global gas mass varies; what *does* alter is the gas fraction at the very highest densities available to the simulations.

4.2 Dependence on the feedback efficiency

Fig. 9 (Fig. 10) shows how the SFH of our HiZ (MW) model depends on the feedback parameters η_p and η_v (equations 5 and 7) and on whether we implement the momentum-feedback continuously or via kicks (left and middle panels). All of the variations are with respect to our standard $\eta_p = \eta_v = 1$ model.

Fig. 9 (left-hand panel) shows that simulations with $\eta_v = 1$ and $\eta_v = 2$ produce very similar SFHs. These two simulations both have $\eta_p = 1$ and thus have the same momentum-injection rate. Physically, the similarity in their SFHs arises because the particles interact with ambient gas and share their momentum efficiently. The end result is that clumps being destroyed by stellar feedback have velocities comparable to the escape velocity from the clump, relatively independent of the initial velocities we input. Fig. 9 also shows a comparison of two different methods of implementing the same momentum flux: particle ‘kicks’ and continuous acceleration (see Section 2.2.2). It is reassuring that these two methods produce quite similar results – this again highlights that the critical parameter is the rate at which momentum is deposited into the ISM, not precisely how it is deposited. The MW-like model in Fig. 10 gives identical conclusions (the dependence is even weaker in this case).

Fig. 9 (middle panel) also compares simulations with varied momentum injection per unit star formation η_p , from $\eta_p = 0.3$ to 10 (all at fixed $\eta_v = 1$). As expected, the quasi-steady SFR decreases as the efficiency of momentum-injection increases. However, the decrease in the SFR is rather mild, with a factor of ~ 2 change in SFR over a factor of 10 in η_p . The same scaling holds in the MW-like model in Fig. 10. Naively one might expect an inverse linear scaling $\dot{M}_* \propto \eta_p^{-1}$ (Thompson et al. 2005). Specifically,

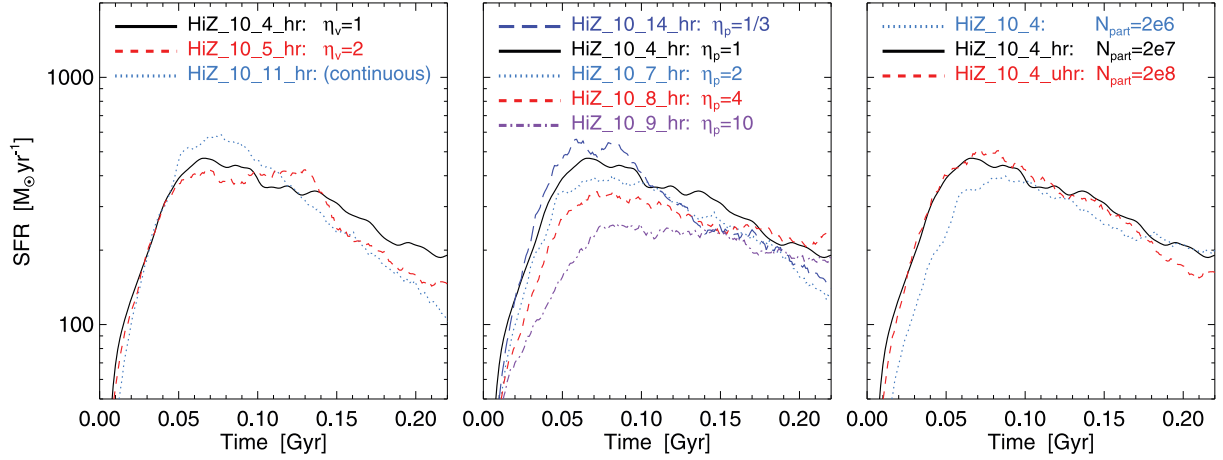


Figure 9. SFR as a function of time for the HiZ model for different feedback parameters and resolution. Left: variations in the initial kick velocities at fixed momentum loading. We also show a simulation with stochastic particle ‘kicks’ replaced by continuous acceleration of all particles. In all of these simulations, the gas shares its momentum with the rest of the surrounding clump and thus produces similar dynamics. Centre: variations in the momentum deposition per unit star formation (η_p ; equation 5). The SFR decreases by less than a factor of 2 over a factor of 10 in η_p . Right: variations in resolution. Increasing the particle number from $\sim 10^6$ to $\sim 10^7$ (our ‘intermediate’ versus ‘high’ resolution) increases the SFR at early times by a moderate amount (~ 20 – 40 per cent). But after about one orbital time, the results are quite similar. Going to yet higher resolution gives nearly identical results.

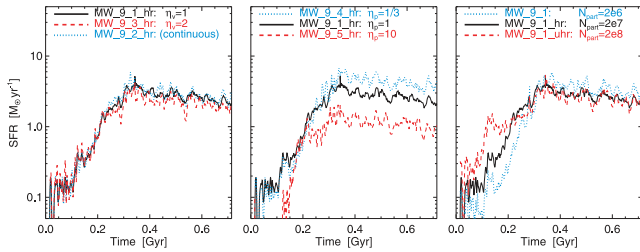


Figure 10. As Fig. 9, but for our MW model. Dependence on η_v and resolution is even smaller than the HiZ case; the dependence on η_p is similar.

the turbulent energy dissipation rate per unit area is

$$\frac{dE}{dA dt} \sim \langle \Sigma \rangle \delta v^2 \Omega \sim G \langle \Sigma \rangle^2 \delta v, \quad (11)$$

where $\langle \Sigma \rangle$ is the mean surface density of the disc and we have assumed $Q \sim 1$ and that turbulence dissipates on a crossing time $\sim h/\delta v \sim \Omega^{-1}$. The total momentum-injection rate scales with the SFR as $\dot{P} \sim (1 + \eta_p \tau_{\text{IR}}) L/c \sim (1 + \eta_p \Sigma \kappa_{\text{IR}}) \epsilon_* \dot{M}_* c$, where $\epsilon_* \approx 4 \times 10^{-4} = L/\dot{M}_* c^2$. If the momentum injection ultimately drives turbulent motions with random velocity δv , the associated energy injection rate is $\sim \dot{P} \delta v$. Balancing this against the dissipation in equation (11), we find that the SFR per unit area Σ_{SFR} is given by

$$\Sigma_{\text{SFR}} \sim \frac{G \langle \Sigma \rangle^2}{\epsilon_* c (1 + \eta_p \tau_{\text{IR}})}. \quad (12)$$

For parameters relevant to Fig. 9, $\eta_p \tau_{\text{IR}} > 1$ and so equation (12) implies that $\dot{M}_* \propto (\tau_{\text{IR}} \eta_p)^{-1}$. This does not, however, imply $\dot{M}_* \propto \eta_p^{-1}$. One reason is that equation (12) neglects the possibility of significant cancellation in colliding/cancelling flows. More importantly, however, for (say) larger η_p , the fraction of mass at high densities decreases because feedback is more effective. This is shown explicitly in Fig. 8 (middle panel): as η_p increases, the density distribution cuts off more sharply at high n . As a result, the optical depth τ_{IR} in the regions of massive star formation decreases. This demonstrates

that the momentum input $\propto \eta_p \tau_{\text{IR}}$, and thus the SFR, must scale sub-linearly with η_p (as in Fig. 9). Assuming that feedback removes gas from high to low density at a rate $\propto \eta_p$, we would expect the fraction of mass at high densities – and the optical depth in those regions – to decrease roughly as η_p^{-1} . This is why both the momentum input $\propto \eta_p \tau_{\text{IR}}$ and the SFR $\propto (\eta_p \tau_{\text{IR}})^{-1}$ have only a weak dependence on η_p . This property of our numerical simulations is one of the most significant differences between our results and previous analytic treatments of star formation regulated by radiation pressure (Thompson et al. 2005). It is important to stress that this self-regulation to achieve the same SFR relatively independent of the feedback parameter η_p is only a property of models in which the momentum-injection rate is proportional to the gas surface density (equation 5); that is, it is only a property of feedback by radiation pressure, not momentum injection associated with SNe or stellar winds.

4.3 Dependence on resolution

Figs 9–10 (right-hand panel) show how the star formation histories of our fiducial $\eta_p = \eta_v = 1$ HiZ and MW models depend on particle number, with $N_{\text{part}} = 2 \times 10^6, 2 \times 10^7$ and 2×10^8 . The basic evolution of the SFR is very similar in all cases. The SFR is ~ 25 – 40 per cent higher at early times in the $N_{\text{part}} = 2 \times 10^7$ simulation relative to $N_{\text{part}} = 2 \times 10^6$, but there is a much smaller change going to yet higher resolution. Moreover, after a few dynamical times, all of the simulations have a comparable SFR. We find similar convergence for different galaxy models and different feedback parameters.

5 THE GLOBAL SCHMIDT-KENNICUTT LAW

Fig. 11 compares the global KS law predicted by simulations with and without our stellar feedback model. We measure $\Sigma_{\text{SFR}} \equiv \dot{M}_*(< R_{\text{sfr}})/\pi R_{\text{sfr}}^2$ as a function of $\Sigma_{\text{gas}} \equiv M_{\text{gas}}(< R_{\text{sfr}})/\pi R_{\text{sfr}}^2$, where R_{sfr} at each time is defined as the half-SFR radius via $\dot{M}_*(< R_{\text{sfr}}) = \dot{M}_*/2$. This radius is chosen to loosely correspond to the half-optical or half-H α radii used in various observational studies, but adopting

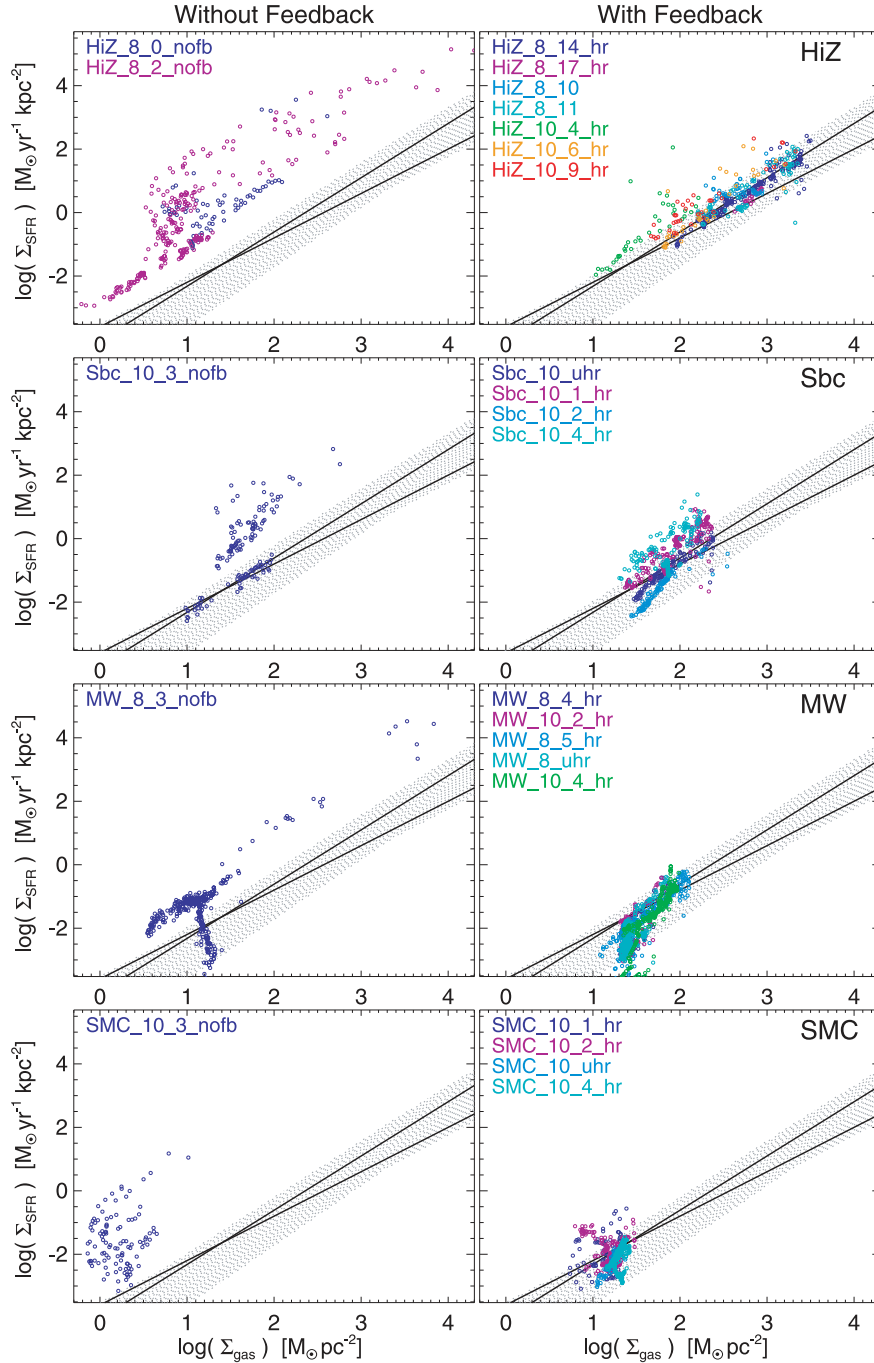


Figure 11. The global KS relation between SFR density and gas surface density in our simulations. Left: without feedback. Right: simulations with our feedback model for a range of parameters (see Table 2). Each row is a different galaxy model (see Table 1). In each panel, a point corresponds to one time snapshot in the simulation, evenly spaced in $\sim 10^6$ yr intervals (starting after two dynamical times). The surface densities are as viewed face-on, averaged within the circular radius that encloses 1/2 of the star formation. Solid lines show the fits to the data in Kennicutt (1998) and updated with high-redshift galaxies by Genzel et al. (2010). Grey shaded region shows the 90 per cent completeness range at each gas surface density from the compilation of the systems observed in those two works as well as the compilations in Bigiel et al. (2008) and Daddi et al. (2010). Without feedback, the gas experiences runaway collapse and is consumed in less than a dynamical time, predicting SFR densities in excess of the observed KS relation by factors of $\sim 100\text{--}10^4$. With feedback, the gas discs quickly self-regulate and reach an approximate equilibrium comparable to that observed.

a different choice (e.g. the half-gas mass radius) primarily shifts the models along the relation. The numerical results are shown every Myr. The numerical results in Fig. 11 are compared with several different observational inferences of the KS relation: the best-fitting

PL relations from low redshift in Kennicutt (1998) and high redshift in Bouché et al. (2007) and Genzel et al. (2010), together with the 10–90 per cent interval of all points from the combined compilations in those studies as well as Bigiel et al. (2008) and Daddi et al.

(2010) (the shaded range).¹⁴ The models with and without feedback have identical initial conditions in each case.

Without feedback our simulations predict a SFR surface density well in excess of the KS law (see also Fig. 4). Absent feedback, the gas cools and cannot avoid runaway collapse; most of the gas is consumed into stars in a single dynamical time, leading to SFR surface densities $\sim 10\text{--}10^4$ times larger than observed.

In contrast, the simulations with feedback lie close to the observed relation at essentially all times. This is true over the range of feedback parameters and resolution we have studied; the runs in Fig. 11 span a range in $\eta_p = 0.5\text{--}10$, $\eta_v = 1\text{--}4$, star formation law variations as in Fig. 6 and resolution ($N_{\text{particles}} \sim 10^5\text{--}10^8$). Varying the simulation parameters for each galaxy model tends to shift the systems along the KS relation, rather than dramatically off the relation. For each galaxy model, there is a broad dynamic range in Σ covered; in particular, the high- z simulations lie on the observed relation over multiple decades in density. The average slope of the relation (if we consider all galaxies together) is quite similar to that observed; however we see that there can be significant variation in the slope within galaxies, also commonly observed (see Bigiel et al. 2008).¹⁵ Altogether, the feedback-regulated simulations lie on the observed KS relation over a dynamic range from $\sim \Sigma_{\text{gas}} \sim 10^7\text{--}10^{10} M_{\odot} \text{ kpc}^{-2}$. The scatter about the Schmidt law predicted is also similar to that observed, about 0.5 dex.

6 DISCUSSION

We have presented a new numerical method for treating stellar feedback in hydrodynamic simulations of galaxies. We have implemented this method in the SPH code GADGET-3 but our approach is general and can be utilized in both Lagrangian and Eulerian codes (see Section 2). Our stellar feedback model is motivated by the physics of feedback in dense environments: under these conditions, gas cools rapidly and the primary dynamical influence of stellar winds, SNe and the stellar radiation field is the momentum they impart to the ISM. In addition to formulating the general method, we have carried out a detailed study of the properties of this stellar feedback model in isolated (non-cosmological) disc galaxy simulations, from models motivated by massive $z \sim 2$ galaxies forming stars at $\sim 100\text{--}300 M_{\odot} \text{ yr}^{-1}$ to models of SMC-like dwarf galaxies. These disc galaxy calculations are not intended to be quantitatively applicable to real systems; rather, they illustrate our method and demonstrate the critical importance of including stellar feedback by momentum injection. In a future paper, we will combine the method developed in this paper with more standard treatments of SN and stellar wind heating, to produce a more comprehensive stellar feedback model.

High-resolution numerical simulations of isolated galaxies and galaxy mergers, as well as cosmological ‘zoom-in’ simulations, can readily resolve the formation of numerous dense gaseous clumps via gravitational instability (provided the cooling to low temperatures $\sim 100 \text{ K}$ is not artificially suppressed); we dub these clumps GMCs although we do not include the physics of molecule formation in

our simulations. In observations of nearby galaxies, most of the star formation occurs in GMCs – this is also true in our simulations – and thus it is important to have at least an approximate model for GMC disruption by stellar feedback.

To model stellar feedback, we implement an on-the-fly clump finding algorithm to identify high-density star-forming clumps (i.e. GMCs). We then deposit momentum into the surrounding gas at a rate proportional to the radiation produced by young stars in the clump; this force is directed radially away from the centre of the GMC. More precisely, the force we apply scales as $\sim \tau_{\text{IR}} L/c$ (equation 5) where τ_{IR} is the optical depth of the clump to IR photons and the stellar luminosity L is calculated as a function of time given the stellar ages using STARBURST99 models. Although our model is quantitatively motivated by radiation pressure on dust, the momentum flux from SNe and massive stellar winds can also be significant. We will study the relative importance of these different feedback mechanisms in detail in a future paper.

The model we have developed is distinct from the stellar feedback models used in most of the galaxy formation literature. First, we input momentum, rather than thermal energy, into the ISM around young stars. The motivation for this choice is that momentum, not energy, is the relevant conserved quantity in dense, rapidly cooling gas. Moreover, the feedback we implement scales with the local surface density of the GMCs, as expected for the radiation pressure produced by stellar photons as they are degraded by dust from the UV to the far-IR (equation 5). As summarized below and in Section 3, we find that this surface density dependence is critical to the evolution of our galaxy models.

In our study of stellar feedback in isolated galaxies, we *do not* ‘turn-off’ hydrodynamic forces, cooling, star formation and/or other physics in the gas to which the feedback is applied. By contrast, many stellar feedback implementations in the galaxy formation literature either turn-off hydrodynamic forces in winds for some free-streaming length (typically such that winds escape the galaxy) or turn-off cooling and star formation in SN-heated gas for some period of time. In such models, the induced velocities on galactic scales are essentially determined by hand (through adjusting the relevant parameters) as is the presence/absence of a global galactic wind driven by stellar feedback. In our model, the single key parameter is the momentum supplied to high-density gas around star clusters – the resulting galaxy-wide turbulence, the properties of galactic winds, etc. are all *predictions* of our model. The model remains ‘sub-grid’, but on the scale of individual molecular clouds rather than the galaxy as a whole.

We are able to directly model the stellar feedback without artificially modifying the underlying equations for several reasons. The high resolution in our simulations allows us to partially resolve the multi-phase ISM structure: since star formation is spatially inhomogeneous, the stellar feedback is as well, which self-consistently maintains a turbulent and multi-phase ISM structure (Fig. 1). Perhaps more importantly, the feedback is momentum-driven and the forces are directed away from the centres of local gas overdensities (GMCs), the sites of massive star formation. As a result, the feedback is effective even in dense regions of the ISM, in which the cooling time is much shorter than the dynamical time. In standard treatments of feedback by SNe, the feedback is inefficient in dense regions because the thermal energy supplied by SNe is rapidly radiated away (Thacker & Couchman 2000; Governato et al. 2007; Ceverino & Klypin 2009; Bournaud et al. 2010; Teyssier et al. 2010; Brook et al. 2011). Thus, many simulations that nominally include stellar feedback do not in fact have feedback that is quantitatively of the correct order of magnitude.

¹⁴ Note that the shaded range falls below the best-fitting PLs at low surface densities because the PL fits did not study the low surface density ‘cut-off’ due to a low molecular fraction.

¹⁵ For example, the MW-like simulation is significantly steeper at low densities than the median relation, but quite similar to spatially resolved observations in M51 (Kennicutt et al. 2007). However, this is the regime where we expect other physics (e.g. the addition of SNe feedback and possibly the effects of detailed molecular chemistry) may become important.

As a first assessment of the implications of our new stellar feedback model, we have used it to study star formation in a wide range of (non-cosmological) disc galaxy models, representing systems ranging from SMC-like dwarfs, to the MW and local LIRGs, through to massive high-redshift gas-rich discs. The discs are initially pressure-supported, but cool rapidly to <100 K and collapse into a wide spectrum of GMCs. Absent stellar feedback, we find that GMCs undergo a runaway gravitational collapse to high density; star formation proceeds on approximately a single galaxy averaged dynamical time (Fig. 4), a result that is dramatically inconsistent with observations (Fig. 11). However, with feedback included, the GMCs dissociate once a modest fraction of their mass has turned into stars and the galaxy develops a turbulent, multi-phase, ISM as long as gas remains. Quantitatively, the turbulence in the ISM maintains marginal stability to self-gravity, i.e. $Q \sim 1$ (Fig. 5). Moreover, the galaxies self-regulate and approach a quasi-steady state SFR that is consistent with the observed KS relation over a dynamic range of several orders of magnitude in surface density (Fig. 11).

Our numerical results are reasonably consistent with the observed global KS relation nearly *independent* of the high-density star formation law used in the simulation (Figs 6 and 11). This is in contrast to many results in the literature, where free parameters in the high-density star formation law are adjusted to approximately reproduce the KS relation (Springel & Hernquist 2003a; Governato et al. 2004; Dubois & Teyssier 2008; Agertz, Teyssier & Moore 2009). A weak dependence of the SFR on the high-density star formation law is important for developing a predictive galaxy formation model. It is otherwise difficult to disentangle results that are due to the physics of star formation and/or feedback from those that are due to particular numerical choices/parameters.

Our star formation model is that gas turns into stars in dense regions above some threshold density ρ_0 at a rate $\dot{\rho}_* \propto \rho^n$. Varying the normalization of this relation (the high-density star formation efficiency) by a factor of ~ 20 , varying ρ_0 by a factor of ~ 100 , and varying the PL index n in the range 1–2 change the quasi-steady-state SFR by $\lesssim 50$ per cent (Fig. 6) (this of course requires that the threshold density be well-resolved). Physically, this weak dependence arises because the condition for quasi-steady state star formation is that the momentum-injection rate by stellar feedback is sufficient to maintain the ISM at $Q \sim 1$. Reaching $Q \sim 1$ requires a particular turbulent velocity δv , and thus a particular momentum-injection rate, for a given set of global galaxy properties (equation 10). Variations in the high-density star formation law are compensated for by slightly more or less gas collapsing to high densities (and differences in how dense the gas becomes before GMCs are dissociated), so as to produce the same momentum-injection rate and hence the same global SFR (Fig. 8).

The key parameter that determines the efficacy of the stellar feedback in our model is the normalization of the momentum-injection rate, η_p (equation 5), where $\dot{p} \sim (1 + \eta_p \tau_{\text{IR}})L/c$; physically, $\eta_p \lesssim 1$ corresponds to photons leaking out of regions with lower-than-average surface densities while $\eta_p \gtrsim 1$ corresponds to the effects of additional momentum sources (e.g. SNe and stellar winds) and/or insufficient resolution of the highest optical depth (τ_{IR}) regions. Numerically, we find less than a factor of 2 change in SFR over a factor of ~ 10 in η_p (Fig. 9). Physically, this is again because maintaining $Q \sim 1$ requires a particular momentum-injection rate and thus a particular SFR. Variations in η_p are compensated for by the surface densities and thus optical depths τ_{IR} reached in dense star-forming clumps, maintaining approximately the same momentum-injection rate independent of η_p (Figs 4 and 8).

Although we have emphasized the importance of momentum input throughout this paper, this is clearly only part of the impact of massive star formation on the ISM of galaxies. Which feedback process is the most important depends on the galaxy mass, gas fraction, etc., and on the specific science question of interest. Heating by photoionization and SNe, and their effect on molecule formation, are critical physics to include in the formation of the first stars as well in studies of lower-density gas characteristic of dwarf galaxies and the outer parts of more massive discs. In the diffuse ISM and the haloes of massive galaxies, additional pressure support from cosmic rays and/or magnetic fields may also be important. The model presented in this paper is most directly applicable to dense gas in the central kpc of massive, enriched and evolved systems, in which cooling times are short and molecular fractions are of the order of unity. Even in these regions, the model here underpredicts the temperatures of the ‘hot’ diffuse ISM ($T \gtrsim 10^6$ K); this gas is likely to be heated by shocks from SNe explosions and fast stellar winds, with $v \sim 1000$ km s $^{-1}$. Although at a given instant, this phase represents only ~ 1 per cent of the gas mass, it can have important effects on the generation of galactic super-winds. In a subsequent paper we will study the combined effect of stellar radiation, stellar winds and SNe, with the goal of developing a more widely applicable stellar feedback model for use in galaxy formation. To extend the study here from idealized discs to discs forming over cosmological time-scales, it will also be important to incorporate the realistic cosmological effects of gaseous haloes and cold-flow accretion as well as galaxy mergers.

ACKNOWLEDGMENTS

We thank Todd Thompson for helpful discussions and for collaboration that motivated this work. We also thank the anonymous referee for a number of thoughtful and useful suggestions. Support for PFH was provided by the Miller Institute for Basic Research in Science, University of California Berkeley. EQ is supported in part by the David and Lucile Packard Foundation. NM is supported in part by the Canada Research Chair program and by NSERC of Canada.

REFERENCES

- Agertz O., Teyssier R., Moore B., 2009, MNRAS, 397, L64
- Ballesteros-Paredes J., Klessen R. S., Mac Low M.-M., Vazquez-Semadeni E., 2007, in Reipurth B., Jewitt D., Keil K., eds, *Protostars and Planets V*. Univ. Arizona Press, Tucson, p. 63
- Besla G., Kallivayalil N., Hernquist L., van der Marel R. P., Cox T. J., Kereš D., 2010, ApJ, 721, L97
- Bigiel F., Leroy A., Walter F., Brinks E., de Blok W. J. G., Madore B., Thornley M. D., 2008, AJ, 136, 2846
- Bouché N. et al., 2007, ApJ, 671, 303
- Boulares A., Cox D. P., 1990, ApJ, 365, 544
- Bournaud F., Elmegreen B. G., Teyssier R., Block D. L., Puerari I., 2010, MNRAS, 409, 1088
- Brook C. B. et al., 2011, MNRAS, 415, 1051
- Bullock J. S. et al., 2001, MNRAS, 321, 559
- Ceverino D., Klypin A., 2009, ApJ, 695, 292
- Cole S., Lacey C. G., Baugh C. M., Frenk C. S., 2000, MNRAS, 319, 168
- Cox T. J., Dutta S. N., Di Matteo T., Hernquist L., Hopkins P. F., Robertson B., Springel V., 2006, ApJ, 650, 791
- Daddi E. et al., 2010, ApJ, 714, L118
- Dalla Vecchia C., Schaye J., 2008, MNRAS, 387, 1431
- Di Matteo T., Springel V., Hernquist L., 2005, Nat, 433, 604
- Dobbs C. L., Burkert A., Pringle J. E., 2011, MNRAS, 413, 2935
- Dubois Y., Teyssier R., 2008, A&A, 477, 79

- Erb D. K., Steidel C. C., Shapley A. E., Pettini M., Reddy N. A., Adelberger K. L., 2006, *ApJ*, 646, 107
- Evans N. J., II, 1999, *ARA&A*, 37, 311
- Evans N. J. et al., 2009, *ApJS*, 181, 321
- Fall S. M., Krumholz M. R., Matzner C. D., 2010, *ApJ*, 710, L142
- Feldmann R., Gnedin N. Y., 2011, *ApJ*, 727, L12
- Förster Schreiber N. M. et al., 2006, *ApJ*, 645, 1062
- Forster Schreiber N. M. et al., 2009, *ApJ*, 706, 1364
- Freyer T., Hensler G., Yorke H. W., 2006, *ApJ*, 638, 262
- Genel S. et al., 2010, *ApJ* (arXiv:1011.0433)
- Genzel R. et al., 2008, *ApJ*, 687, 59
- Genzel R. et al., 2010, *MNRAS*, 407, 2091
- Genzel R. et al., 2011, *ApJ*, 733, 101
- Goodman A. A., Pineda J. E., Schnee S. L., 2009, *ApJ*, 692, 91
- Governato F. et al., 2004, *ApJ*, 607, 688
- Governato F., Willman B., Mayer W., Brooks A., Stinson G., Valenzuela O., Wadsley J., Quinn T., 2007, *MNRAS*, 374, 1479
- Guo Q., White S., Li C., Boylan-Kolchin M., 2010, *MNRAS*, 404, 1111
- Hernquist L., 1990, *ApJ*, 356, 359
- Hernquist L., 1993, *ApJ*, 404, 717
- Hopkins P. F., Hernquist L., Martini P., Cox T. J., Robertson B., Di Matteo T., Springel V., 2005, *ApJ*, 625, L71
- Katz N., Weinberg D. H., Hernquist L., 1996, *ApJS*, 105, 19
- Kennicutt R. C., Jr, 1998, *ApJ*, 498, 541
- Kennicutt R. C., Jr, et al., 2007, *ApJ*, 671, 333
- Kereš D., Katz N., Davé R., Fardal M., Weinberg D. H., 2009, *MNRAS*, 396, 2332
- Kroupa P., 2002, *Sci*, 295, 82
- Krumholz M., Burkert A., 2010, *ApJ*, 724, 895
- Krumholz M. R., Matzner C. D., 2009, *ApJ*, 703, 1352
- Krumholz M. R., Tan J. C., 2007, *ApJ*, 654, 304
- Law D. R., Steidel C. C., Erb D. K., Larkin J. E., Pettini M., Shapley A. E., Wright S. A., 2009, *ApJ*, 697, 2057
- Leitherer C. et al., 1999, *ApJS*, 123, 3
- Leroy A. K., Walter F., Brinks E., Bigiel F., de Blok W. J. G., Madore B., Thornley M. D., 2008, *AJ*, 136, 2782
- Lopez L. A., Krumholz M. R., Bolatto A. D., Prochaska J. X., Ramirez-Ruiz E., 2011, *ApJ*, 731, 91
- McKee C. F., Ostriker J. P., 1977, *ApJ*, 218, 148
- Mashchenko S., Wadsley J., Couchman H. M. P., 2008, *Sci*, 319, 174
- Matzner C. D., 2002, *ApJ*, 566, 302
- Moster B. P., Somerville R. S., Maubetsch C., van den Bosch F. C., Macciò A. V., Naab T., Oser L., 2010, *ApJ*, 710, 903
- Murray N., 2009, *ApJ*, 691, 946
- Murray N., 2011, *MNRAS*, 417, 133
- Murray N., Quataert E., Thompson T. A., 2005, *ApJ*, 618, 569
- Murray N., Quataert E., Thompson T. A., 2010, *ApJ*, 709, 191
- Nagamine K., 2010, *Adv. Astron.*, 2010
- Navarro J. F., Frenk C. S., White S. D. M., 1996, *ApJ*, 462, 563
- Noeske K. G. et al., 2007, *ApJ*, 660, L47
- O'Shea B. W., Nagamine K., Springel V., Hernquist L., Norman M. L., 2005, *ApJS*, 160, 1
- Oppenheimer B. D., Davé R., 2008, *MNRAS*, 387, 577
- Ostriker E. C., Stone J. M., Gammie C. F., 2001, *ApJ*, 546, 980
- Powell L. C., Slyz A., Devriendt J., 2011, *MNRAS*, 414, 3671
- Power C., Navarro J. F., Jenkins A., Frenk C. S., White S. D. M., Springel V., Stadel J., Quinn T., 2003, *MNRAS*, 338, 14
- Robertson B. E., Kravtsov A. V., 2008, *ApJ*, 680, 1083
- Robertson B., Hernquist L., Cox T. J., Di Matteo T., Hopkins P. F., Martini P., Springel V., 2006, *ApJ*, 641, 90
- Saitoh T. R., Daisaka H., Kokubo E., Makino J., Okamoto T., Tomisaka K., Wada K., Yoshida N., 2008, *PASJ*, 60, 667
- Sales L. V., Navarro J. F., Schaye J., Vecchia C. D., Springel V., Booth C. M., 2010, *MNRAS*, 409, 1541
- Salim S. et al., 2007, *ApJS*, 173, 267
- Sánchez-Salcedo F. J., Vázquez-Semadeni E., Gazol A., 2002, *ApJ*, 577, 768
- Sanders D. B., Mirabel I. F., 1996, *ARA&A*, 34, 749
- Scannapieco C., Tissera P. B., White S. D. M., Springel V., 2008, *MNRAS*, 389, 1137
- Schaye J. et al., 2010, *MNRAS*, 402, 1536
- Schruba A., Leroy A. K., Walter F., Sandstrom K., Rosolowsky E., 2010, *ApJ*, 722, 1699
- Slyz A. D., Devriendt J. E. G., Bryan G., Silk J., 2005, *MNRAS*, 356, 737
- Somerville R. S., Primack J. R., 1999, *MNRAS*, 310, 1087
- Springel V., 2005, *MNRAS*, 364, 1105
- Springel V., Hernquist L., 2002, *MNRAS*, 333, 649
- Springel V., Hernquist L., 2003a, *MNRAS*, 339, 289
- Springel V., Hernquist L., 2003b, *MNRAS*, 339, 312
- Springel V., Di Matteo T., Hernquist L., 2005, *MNRAS*, 361, 776
- Tacconi L. J. et al., 2006, *ApJ*, 640, 228
- Tacconi L. J. et al., 2010, *Nat*, 463, 781
- Tasker E. J., Tan J. C., 2009, *ApJ*, 700, 358
- Teyssier R., Chapon D., Bournaud F., 2010, *ApJ*, 720, L149
- Thacker R. J., Couchman H. M. P., 2000, *ApJ*, 545, 728
- Thompson T. A., Quataert E., Murray N., 2005, *ApJ*, 630, 167
- Thornton K., Gaudlitz M., Janka H., Steinmetz M., 1998, *ApJ*, 500, 95
- Truelove J. K., Klein R. I., McKee C. F., Holliman J. H., II, Howell L. H., Greenough J. A., 1997, *ApJ*, 489, L179
- Vitvitska M., Klypin A. A., Kravtsov A. V., Wechsler R. H., Primack J. R., Bullock J. S., 2002, *ApJ*, 581, 799
- Williams J. P., McKee C. F., 1997, *ApJ*, 476, 166
- Wise J. H., Abel T., 2008, *ApJ*, 685, 40
- Wong T. et al., 2008, *MNRAS*, 386, 1069
- Younger J. D., Hopkins P. F., Cox T. J., Hernquist L., 2008, *ApJ*, 686, 815
- Zuckerman B., Evans N. J., II, 1974, *ApJ*, 192, L149

APPENDIX A: ADDITIONAL NUMERICAL TESTS

In this Appendix, we discuss a number of additional numerical tests performed to ensure that our conclusions are not sensitive to the precise implementation of the feedback algorithm.

Fig. A1 shows examples in which we modified the friends-of-friends search used to identify the nearby density peak that is the origin for our feedback (see Section 2.2.1). Specifically, we varied the parameter N_{sml} between 1 and 5 (our standard model adopts $N_{\text{sml}} = 3$) – this defines the number of smoothing lengths in which to search for a more dense gas particle in each iteration. Within this range we do not see significant differences in most of the identified density peaks; nor is there a significant effect on the SFH (Fig. A1). We have also modified the resolution-dependent pressure floor used to avoid artificial collapse, through the parameter N_{Jeans} which represents the minimum number of smoothing lengths which resolve the Jeans length (equation 1). Because all of our feedback-regulated runs have large feedback-induced random velocities, this pressure floor makes no significant difference in these cases (see Fig. A1). It does, however, determine the smallest scale of resolved structure in simulations without feedback (see e.g. Robertson & Kravtsov 2008).

To reduce the code run-time and ensure that feedback is relatively local to massive stars, we only apply the feedback to gas particles within $N_* = 3$ smoothing lengths of any star particle (Section 2.2.2). We have experimented with this value in the range 2–20 (the latter value including almost all of the gas). Because the optical depths and momentum deposition are dominated by the gas closest to the stars, this choice has very small effects on the ISM properties and SFH (Fig. A1).

One aspect of our method that can have a more significant influence on the results is the direction in which particles are accelerated when the feedback is applied. In the standard model, we accelerate

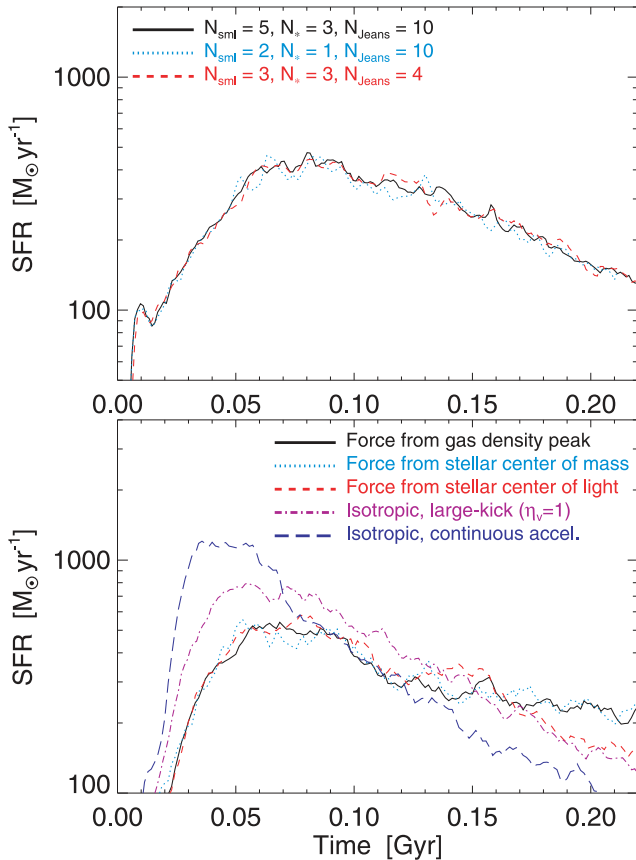


Figure A1. Example star formation histories for the HiZ galaxy model for variations in the details of our numerical method. Top: otherwise identical simulations with different choices of N_{sml} (linking length for clump finder), N_* (number of lengths to smooth/cut the radiation field) and N_{Jeans} (numerical pressure support to prevent artificial fragmentation). Bottom: otherwise identical simulations with variations in the direction in which the feedback is applied. Applying the force radially outwards from the nearest gas density peak, stellar centre of mass or centre of light give nearly identical results. The ‘isotropic’ models choose the direction of each kick randomly. When individual kicks are relatively rare and large ($\eta_v \gtrsim 1$), this is somewhat less efficient than radial kicks but still stirs turbulence and slows down star formation. By contrast, in the limit of continuous acceleration, random isotropic forces cancel, impart little net momentum, and the SFR is only a factor of ~ 2 smaller than that found in the absence of feedback (Fig. 4).

particles away from the gas density peak identified in the friends-of-friends search (Section 2.2.2). We have experimented with changing the origin for this force to be the centre of mass of the stars or gas or the centre of luminosity of the star-forming clump. We have also considered models in which the force vector is oriented along the local density gradient (appropriate in principle for arbitrary geometries, in the regime where τ_{IR} falls below unity along that gradient). We find that these models give nearly indistinguishable results, as is shown in Fig. A1. This is essentially because most of the stars are concentrated near the clump centre (by any of these metrics) for most of the time when feedback is important. On small scales in galaxies (or *interior* to GMCs), however, the dynamical time can be much shorter than the lifetime of massive stars, and so it is possible that large separations could arise between massive stars and the gas from which they formed. In this case, it would be better to determine the direction of the force using the local peak in stellar luminosity.

We have also considered experiments in which we completely ignore the clump density information and kick particles with isotropic,

random directions (rather than away from clump centres). In our standard model ($\eta_v = 1$), kicks are somewhat rare but have large initial velocities, so the coherent momentum imparted with each kick is still large (even if it is randomly directed). In this case, the feedback is somewhat less effective than in our standard model and so the SFR is somewhat larger (Fig. A1). If the individual kicks particles receive are much smaller (but more frequent), the coherent momentum imparted will be reduced if each is independently randomly oriented. As a result, in the limit in which we continuously accelerate particles in random directions (rather than imparting discrete kicks), we find that the feedback has little effect. The SFH is similar to models with no feedback (Fig. A1). This highlights the importance of properly applying the feedback radially away from the centre of mass/luminosity of massive star clusters.

There are other aspects of our simulations that are uncertain, independent of the stellar feedback model. For example, our cooling function at low temperatures is not exact, since we do not explicitly follow chemical networks. We have therefore considered various arbitrary changes to the cooling function: setting $\Lambda(T)$ below 10^4 K to a constant median value, or simply forcing all gas at high densities to a minimum temperature ~ 100 K. These introduce <20 per cent changes in, e.g., the SFH, since in all cases the cooling time is short relative to the dynamical time. On the other hand, removing fine structure cooling entirely (effectively producing a cooling floor at 10^4 K) dramatically changes the behaviour in the MW, Sbc and SMC cases, since this temperature floor is sufficient to artificially prevent collapse to high densities. However, it makes little difference in the HiZ case because the requirement for $Q > 1$ is $c_s \gtrsim 30\text{--}50$ km s $^{-1}$.

APPENDIX B: THE EFFECTS OF PHOTON ‘LEAKAGE’

A subtle complication in modelling the effects of radiation pressure arises if the ISM is truly inhomogeneous on all scales, including those well below what we model. A patch of ISM that appears smooth in the simulations, with some average optical depth τ_0 , may more accurately (at infinite resolution) exhibit a distribution of local columns, including some optically thin lines of sight that could, in principle, allow photons to ‘leak out’ at a rate much higher than the nominal $\exp(-\tau_0)$ expectation. This would potentially lower the effective ‘boost’ to the radiation pressure from $\tau_0 L/c$ to some $\tau_{\text{eff}} L/c$. It is straightforward to show that leakage will not significantly change the total energy absorbed and therefore the IR luminosity density – once τ_0 is large, it is generically true for essentially any realistic distribution of optical depths that *most* of the incident optical/UV radiation is initially absorbed (whether the escape fraction is a few tens of per cent or vanishingly small makes only a tens of per cent change to L_{IR}). The concern is rather that IR photons will tend to escape along optically thin sightlines before they scatter sufficiently numerous times to impart the full $\sim \tau_0$ momentum boost. Krumholz & Matzner (2009), for example, argue that the latter effect means that the effective τ_{eff} can never be larger than a few, even when $\tau_0 \gg 1$. But they do so by assuming an order-unity fraction of un-obscured sightlines, independent of τ_0 . We therefore consider this effect in more detail in this Appendix.

As discussed in the text, the case of a perfectly homogenous density distribution with a source at the centre is trivial. The opacity along all sightlines is τ_0 , so the photon scatters an average of $N = \tau_0^2$ times as it performs a random walk to diffuse out of the sphere. For a random walk, the net momentum flux directed radially away from the central source is just $\tau_{\text{eff}} L/c$ where $\tau_{\text{eff}} = \sqrt{N}$, which in this case gives $\tau_{\text{eff}} = \tau_0$.

But now consider a case with an inhomogeneous density distribution. Unfortunately in general, calculating the precise τ_{eff} for any inhomogeneous density distribution is complex and cannot be solved analytically – it requires a full radiative transfer solution for each specific density distribution. However, we can make considerable progress and obtain reasonably general scaling laws with some simplifying assumptions. Consider a ‘cloud’ of ISM with a well-defined mean τ_0 (which we can measure easily in the simulations) enclosing a source at its centre; for convenience (with no loss of generality) define the cloud radius to be $\ell_0 = 1$. Now define the ‘true’ distribution of optical depths across all sightlines within the cloud to be $dP(\tau|\tau_0)$. Finally, assume that the cloud is self-similar with structure on all scales. In this limit, the distribution of local densities or $d\tau/d\ell$ (where ℓ is the distance along a line of sight) is just $dP(d\tau/d\ell) = dP(\tau/\ell_0|\tau_0/\ell_0) = dP(\tau|\tau_0)$. We can perform the following relatively simple calculation: take a population of photons starting at the centre, with initial random directions. For each, draw a random $d\tau/d\ell$ (equivalently, line-of-sight-averaged density), and determine in standard Monte Carlo fashion the distance the photon travels before being absorbed (for a uniform random variable p between zero and unity, $\Delta\ell = -\ln(1-p)/[d\tau/d\ell]$). At each ‘scattering’, determine a new random direction for the photon to be re-emitted, and record the locally coupled momentum as the negative of the change in the photon momentum. This is iterated until all photons escape the sphere; using a large Monte Carlo sample of ‘photons’, then, we can determine quantities such as the average number of scatterings $\langle N \rangle$ and the average momentum imparted (or effective boost τ_{eff}).¹⁶

Of course, we still need to specify some distribution $dP(\tau|\tau_0)$. Fortunately, we can make a reasonable estimate: in ultra-high-resolution simulations, we can calculate, for example, the form of $dP(\tau|\tau_0)$ for each molecular cloud in the simulation, using a large number (~ 1000) of lines of sight and integrating the simulation column along each sightline. In Section 2.2.2, we discuss this process and note that the resulting column density distribution on a per-cloud basis can be well-approximated by a near-universal function

$$dP(\tau|\tau_0) \approx \frac{1}{2\sigma} \exp\left(-\frac{|\ln(\tau/\tau_0)|}{\sigma}\right) \frac{d\tau}{\tau} \quad (\text{B1})$$

with σ (the standard deviation) ranging from 0.25 to 1.0 (0.1 to 0.4 dex) with a median $\sigma = 0.5$ (0.22 dex). This is very similar to the distribution of columns estimated in much higher resolution simulations of individual GMCs and sub-cloud clumps (often with very different physics included; see e.g. Ostriker et al. 2001), and to observational estimates of the column density distribution across observed GMCs (Wong et al. 2008; Goodman et al. 2009).

Note that this distribution is exponential in $\log(\tau)$ – really, the key behaviour is that the number of sightlines at small or large τ falls off as a *PL* in (τ/τ_0) , rather than an exponential or LN. This is important, as we will see below.

Given some σ , then, it is straightforward to perform the Monte Carlo calculation of τ_{eff} described above. Fig. B1 shows the coupled momentum τ_{eff} as a function of the average τ_0 , for a few values of σ . At very low τ_0 , the coupled boost drops off rapidly because a large fraction of sightlines are optically thin – but in this case, the ‘boost’ is negligible in either case (with or without leakage). At low to moderate τ_0 , the effective τ_{eff} rises with τ in a linear fashion

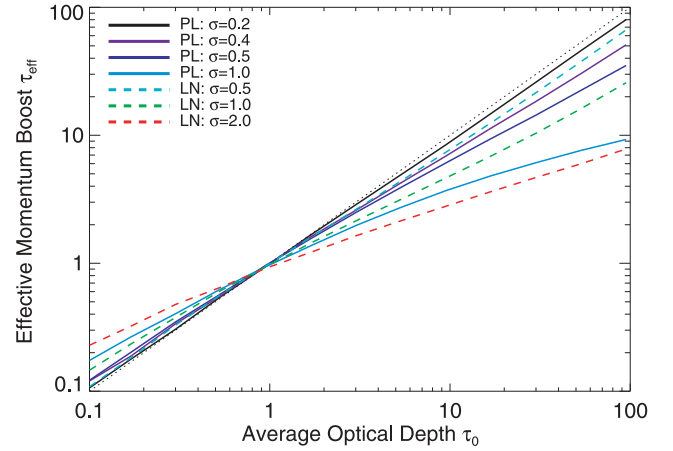


Figure B1. Modified coupling of photon momentum in a self-similar, ‘leaky’ medium with a broad density distribution. The true ‘boost’ to the coupling τ_{eff} defined such that $\dot{P} = \tau_{\text{eff}} L/c$ is plotted as a function of the mean τ_0 , for a source at the centre of a medium with a random distribution of densities that obeys a PL (equation B1) or LN (equation B3) PDF with logarithmic dispersion σ . Dotted line shows $\tau_{\text{eff}} = \tau_0$, the expectation for a completely homogeneous medium. For $\sigma < 1$ in the LN model, or < 0.5 in the PL model, $\tau_{\text{eff}} \propto \tau_0$ (with relatively small normalization corrections comparable to small variations in our η_p parameter). At larger dispersion, the scaling becomes sub-linear, with $\tau_{\text{eff}} \propto \tau_0^{1/2\sigma}$ (PL) or $\tau_{\text{eff}} \propto \tau_0^{\ln \tau_0 / 4\sigma^2}$ (LN). The dispersion in ultra-high-resolution simulations (and observations) corresponds to $\sigma \approx 0.5$.

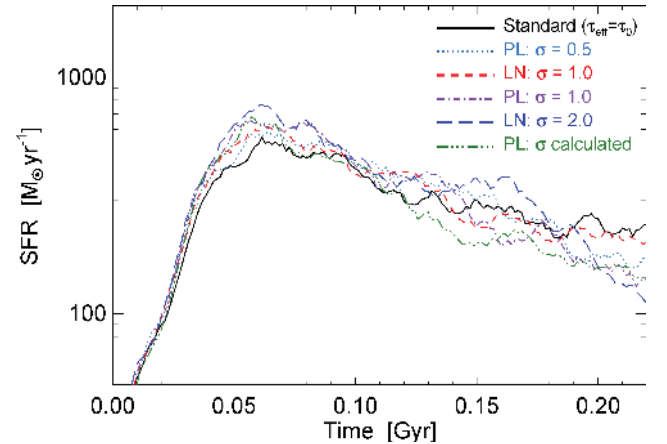


Figure B2. Effects of IR photon ‘leakage’ as calculated in Fig. B1 on the SFH of simulated galaxies (here the HiZ model). We compare our standard model ($\tau_{\text{eff}} = \tau_0$) to models using the calculated $\tau_{\text{eff}}(\tau_0)$ from Fig. B1, for an assumed universal σ and functional form of the density distribution as in that figure. We also compare a model with the PL/exponential distribution (equation B1) and σ calculated on-the-fly as the dispersion in $\ln(\rho)$ within the identified clump radii R_{clump} . Larger dispersion in columns leads to more leakage and higher SFRs, but the effect is weak and, in the regime of interest here, similar to a choice of η_p slightly somewhat less than unity.

as we would naively expect. At high- τ_0 , however, the behaviour depends on σ , with a critical change in behaviour around $\sigma = 1/2$. This can be understood from the form of $dP(\tau|\tau_0)$.

For the distribution in equation (B1), the fraction of optically thin sightlines ($\tau < 1$) scales simply as

$$f_{\text{thin}} = \frac{1}{2\sigma} \tau_0^{-1/\sigma}. \quad (\text{B2})$$

¹⁶ Specifically, we are interested in the net momentum imparted radially away from the centre. As expected, all other components of the coupled momentum average to zero.

So, the average number of scatterings needed before a photon will ‘find’ an optically thin sightline – and therefore have a high probability of escaping the cloud – is, crudely, $N_{\text{thin}} \sim 1/f_{\text{thin}} \propto \tau_0^{1/\sigma}$. On the other hand, the number of scatterings needed before the photon would diffuse out of the cloud assuming it did *not* find an optically thin sightline is just $N_{\text{diffuse}} \sim \tau_0^2$. What matters for the behaviour at high- τ_0 is just this PL falloff (exactly how we model the ‘core’ and high- τ part of the PDF make almost no difference to the values of τ_{eff} plotted in Fig. B1 at high- τ_0).

If $\sigma < 1/2$, then N_{thin} grows more rapidly than N_{diffuse} ; in other words, the number of optically thin sightlines falls off sufficiently rapidly at large τ_0 than the typical photon will undergo its expected number of $\sim \tau_0^2$ scatterings to diffuse out before it ‘leaks’ out of an optically thin sightline, so that the coupled momentum $\tau_{\text{eff}} \propto \sqrt{N} \propto \tau_0$. There is a linear normalization correction to τ_{eff} , which we can estimate analytically by considering the average distance travelled between scatterings, i.e. $\langle \Delta \ell \rangle \propto \langle \tau^{-1} \rangle$ – this accounts for the fact that, on average, slightly more thin or thick sightlines allow for fewer or more scatterings before escape: we obtain the result that, for $\tau_0 \gg 1$, $\tau_{\text{eff}} \rightarrow (1 - \sigma^2) \tau_0$.

If $\sigma > 1/2$, however, then N_{diffuse} grows more rapidly than N_{thin} ; so the average photon will ‘leak out’ after just N_{thin} scatterings, before it can couple the full $\tau_0 \sim \sqrt{N_{\text{diffuse}}}$ ‘boost.’ The actual coupled momentum should instead scale as $\tau_{\text{eff}} \sim \sqrt{N_{\text{thin}}}$, which gives $\tau_{\text{eff}} \propto \tau_0^{1/2\sigma}$. Again, we can analytically estimate the pre-factor for $\tau_0 \gg 1$, and obtain $\tau_{\text{eff}} \rightarrow \sqrt{\sigma/2} \Gamma[1/\sigma] \tau_0^{1/2\sigma}$. The important point is that in this regime, the scaling is *sub-linear* in τ_0 . There is still an approximately linear regime at moderate τ_0 , but for very high τ_0 , the ‘boost’ becomes more limited.

We stress that this behaviour arises because the assumed $dP(\tau|\tau_0)$ behaves as a PL at low τ/τ_0 – in other words, this allows for essentially the maximal ‘long tail’ of low- τ sightlines towards a central source with high average optical depth. Since $dP(d\tau/d\ell|\tau_0/\ell_0)$ reflects the local three-dimensional density distribution, it might for example be more natural to assume it should have an LN form:

$$dP(\tau|\tau_0) \approx \frac{1}{\sigma\sqrt{2\pi}} \exp\left(-\frac{\ln(\tau/\tau_0)^2}{2\sigma^2}\right) \frac{d\tau}{\tau}. \quad (\text{B3})$$

The results of assuming this distribution are shown in Fig. B2. Given this distribution, the high- τ_0 limit essentially always gives a linear scaling $\tau_{\text{eff}} \propto \tau_0$. The reason is obvious given the arguments above – for an LN, the fraction of low- τ sightlines will decline much faster than a PL, so independent of σ , the probability of finding optically thin sightlines at $\tau \ll \tau_0$ will fall much faster than τ_0^{-2} . For $\sigma \lesssim 1$, then, $\tau_{\text{eff}} \rightarrow \tau_0$ when $\tau_0 \gg 1$. At very large σ or more moderate τ_0 , of course, $\tau \sim 1$ may still fall within the ‘core’ of the LN. For equation (B3), the fraction of optically thin sightlines when $\tau_0 \gg 1$ is $f_{\text{thin}} = (\sigma/\sqrt{2\pi}) \ln^{-1}(\tau_0) \tau_0^{-(\ln \tau_0)/(2\sigma^2)}$, or $f_{\text{thin}} \propto \tau_0^{-(\ln \tau_0)/(2\sigma^2)}$. The requirement that this fraction drop faster than τ_0^{-2} (to give $\tau_{\text{eff}} \sim \tau_0$) therefore becomes $\tau_0 \gtrsim \exp(4\sigma^2)$. For the reasonable values of σ up to the order of unity, this is easily satisfied for high- τ_0 . But if σ were very large (say ~ 2), this rapidly becomes extremely large, and so we return to the $N_{\text{thin}} < N_{\text{diffuse}}$ limit, and obtain the sub-linear scaling $\tau_{\text{eff}} \rightarrow (2\pi)^{1/4} [\ln(\tau_0)/\sigma]^{1/2} \tau_0^{(\ln \tau_0)/4\sigma^2}$. Even in this regime, however, it is worth noting that at very high τ_0 , the PL model of equation (B1) still has a larger optically thin fraction – for a fixed σ , that model gives a maximal effect of leakage.

We can test the effects of this in our simulations by replacing the standard boost of τ_0 with one of the appropriate τ_{eff} calculated above with some fixed σ (using the curves in Fig. B1 to define an interpolation table). Obviously, for either distribution, a value of $\sigma < 0.5$ will make no difference to any of our conclusions because

$\tau_{\text{eff}} \propto \tau_0$: the normalization correction is completely equivalent to variations in η_p , discussed in the text (and in the regime of very low τ , the boost scaling is not important). Moreover, for an LN distribution, any $\sigma < 1$ will yield identical results. We therefore consider experiments with the exponential/PL distribution and assumed $\sigma = 0.5, 1.0$ and LN distribution with assumed $\sigma = 1.0, 2.0$. For the PL distribution with $\sigma = 0.5$ or LN with $\sigma = 1.0$, τ_{eff} begins to deviate from τ_0 at $\tau_0 \gg 1$, but the differences are sufficiently small that we do not see a large effect (they are roughly comparable to choices of $\eta_p = 2/3$ and $=1/2$, respectively, and so change the expected SFRs only at the 20–30 per cent level). For the very large choices of σ , however, we do expect and see some deviations. The equilibrium SFR is systematically larger by a factor of ~ 2 , similar to a small $\eta_p \sim 1/4$ (since the median $\tau_{\text{IR}} \sim 30$ –50 becomes $\tau_{\text{eff}} \sim 10$ here, this is expected). Visual inspection in these cases also confirms there are some small sub-regions in the galaxy nucleus where the gas consumption is near-runaway (these do not contain much of the mass, but they have the highest densities, $\tau_{\text{IR}} \sim 100$). Finally, we have also considered runs in which the PL model is adopted, but with σ taken from the local gas properties. Specifically, we take all of the gas inside the identified clump radius R_{clump} , and (knowing the density of each particle) compute the dispersion in $\ln(\rho)$ which we use as σ . We also add in quadrature a minimum $\sigma = 0.25$ (0.1 dex) which is about the minimum dispersion we see in ultra-high-resolution simulations (in order to again be conservative and allow for significant leakage). The results of this run are quite similar to our default $\tau_{\text{eff}} = \tau_0$ model and/or the $\sigma = 0.5$ model, which we expect since, as noted in the text, the typical σ we measure in simulation clumps is about 0.5. It is worth noting though, that the typical σ increases as we consider older and older stars, as a consequence of feedback in earlier stages driving out gas and ‘punching holes’ in the gas distribution. Of course, the mean optical depth is also going down here, and we saw in the text that stars with the youngest ages $\lesssim 1$ Myr dominate the radiative momentum input. So accounting for leakage accelerates the rate at which old stars luminosity can escape without coupling in the IR, but does not change our conclusions.

We should also emphasize that other sub-grid effects could in fact *raise* τ_{eff} at fixed τ_0 . This includes some non-trivial geometric cases where photons can be more efficiently trapped. Also, recall that we define τ_0 in the model as the globally averaged τ out to a given radius $\propto M_{\text{enc}} R^{-2}$, rather than the line-of-sight-integrated τ . If the gas within R is distributed with any average density profile that rises towards the stars, the appropriate τ_{eff} should be larger than that in Fig. B1 [for a pure PL profile $\rho \propto r^{-\alpha}$, this gives a factor $\propto 1/(1 - \alpha)$ which is actually divergent for $\alpha > 1$]. In fact, if we calculate the true median line-of-sight-integrated τ in our ultra-high-resolution simulations and compare it to the adopted τ_0 , the typical correction would amount to a ‘boost’ of $\eta_p \approx 2$. Moreover, if we under-resolve collapse such that the gas ‘should’ collapse a factor $\sim \psi$ further in radius than our resolution limit allows, then $\tau_{\text{eff}} \sim \psi^2 \tau_0$ would be appropriate. It is difficult, therefore, to identify a ‘more accurate’ model than our $\tau_{\text{eff}} \propto \tau_0$ that is robust at the factor of ~ 2 level.

We therefore conclude that photon leakage is unlikely to qualitatively change our conclusions, given observationally and theoretically realistic distributions of column densities towards optically thick sources. However, it might be important in the most dense systems observed: starburst nuclei and AGN. The average IR optical depths in these regions can reach values > 100 . The absolute value of the correction to τ_{eff} here could therefore be quite large – a factor of ~ 10 rather than ~ 2 , if σ is sufficiently large. Moreover, the sub-linear behaviour of τ_{eff} could be very important, because these regions both have high- τ_0 and have dynamical times that are

short relative to the stellar evolution time-scale. In this joint limit, the luminosity required to support the system is $\tau_{\text{eff}} L/M \propto (M/R^2)$ or $L/M \propto \tau_0/\tau_{\text{eff}}$. When we are in the linear regime ($\tau_{\text{eff}} \propto \tau_0$), either because of low σ or low $\tau_0 \lesssim 10$, this implies that the system can self-regulate on both small and large scales once a fraction (a few per cent) of the mass becomes stars. However, if τ_{eff} is significantly sub-linear, then the L/M needed to stabilize is a rising function of τ – in other words, the system is vulnerable to runaway collapse (Fall, Krumholz & Matzner 2010). Such collapse could be quite interesting in these regions, however, since it would proceed with regions

above a critical τ_0 running away to turn entirely into stars, while neighbouring regions that had smaller τ_0 do not collapse – and once the global L/M reached a given threshold, the low-density regions would be self-regulated. One might imagine a regime of global self-regulation on these scales, but without *local* self-regulation, perhaps making these regimes particularly interesting for the formation of globular clusters, dwarf galaxy nuclei and/or super star clusters.

This paper has been typeset from a $\text{\TeX}/\text{\LaTeX}$ file prepared by the author.